LHC Project Note 418

May 27, 2009

rainer.wanzenberg@desy.de

Calculation of Higher Order Modes and Wakefields for the Vacuum Chamber of the CMS Experiment at the LHC

R. Wanzenberg
DESY, Notkestr. 85, 22603 Hamburg, Germany

Keywords: higher order modes, wakefields, CMS vacuum chamber

Summary

The trapped Higher Order Modes (HOMs) in the vacuum chamber of the CMS experiment at the LHC have been investigated using a geometrical model which closely reflects the presently (in 2008) installed vacuum chamber. The basic rf-parameters of the HOMs including the frequency, loss parameter, G_1 and the Q-value together with extensive graphical representations of the longitudinal electrical fields are provided. To also cover transient effects the short range wakefields and the total loss parameter have been calculated, too. Most numerical calculations have been performed with the computer code MAFIA. The obtained data are intended to be included into the impedance database of the LHC.

1 Introduction

1.1 The LHC accelerator

The Large Hadron Collider (LHC), which is installed in the 27 km long tunnel that had been previously been used for the Large Electron Positron collider (LEP), is intended to provided proton-proton collisions with a center-of-mass energy of 14 TeV and a luminosity of $1.0 \cdot 10^{34}$ cm^{-2} s^{-1}. The main parameters of the accelerator for luminosity operation are shown in Table 1, and have been compiled from Ref. [1]. The LHC has an 8-fold symmetry with eight arc sections and eight straight sections which contain experiments and systems for the machine operation. The two counter circulating proton beams will collide at the interaction points (IPs) in sector 1 and 5, where the experiments ATLAS (IP 1) and CMS (IP 5) have been installed.

The electromagnetic interaction of the proton beam with parasitic or higher order modes (HOMs) in the vacuum chamber of the CMS experiment is investigated in this paper. A geometrical model of the CMS chamber which closely reflects the presently (in 2008) installed

Parameter	Symbol	Value	Unit
Proton energy	E_p	7000	GeV
Ring circumference	C_R	26658.883	m
Bending radius	ρ_D	2803.95	m
RMS beam size at IP1 and IP5	$\sigma_{x,y}$	16.7	μm
Peak luminosity in IP1 and IP5	$\hat{\mathcal{L}}$	$1.0 \cdot 10^{34}$	cm^{-2} s^{-1}
Momentum compaction	α_p	3.225	10^{-4}
Horizontal tune	ν_x	64.31	
Vertical tune	ν_y	59.32	
Transverse normalized emittance	$\gamma\epsilon_{x,y}$	3.75	mm mrad
Revolution frequency	f_R	11.245	kHz
RF frequency	f_{rf}	400.8	MHz
Total RF voltage	V_{rf}	16	MV
Harmonic number	h	35640	
Synchrotron frequency	f_s	21.4	Hz
RMS bunch length	σ_z	7.55	cm
Number of bunches	N_b	2808	
Number of particles per bunch	N_0	$11.5 \cdot 10^{10}$	
Charge of one bunch	q_b	18.4	nC
Circulating beam current	I_{tot}	0.582	A

Table 1: Main parameters of the LHC at collision energy [1].

vacuum chamber is described in the next subsection. Wakefields and HOMs have been calculated for previous versions of the CMS vacuum chamber in [2, 3, 4, 5].

For the wakefield calculations it is assumed that the charge density is a Gaussian distribution with an RMS bunch length of $\sigma_z = 7.5$ cm:

$$\rho(z) = q_b\, g(z), \quad \text{with} \quad g(z) = \frac{1}{\sigma_z}\frac{1}{\sqrt{2\,\pi}} \exp\left(-\frac{1}{2}\left(\frac{z}{\sigma_z}\right)^2\right). \tag{1}$$

The Gaussian function g is plotted in Fig. 1, while the Fourier transform of g and the spectral power density h, defined as

$$\begin{aligned} \widetilde{g}(\omega) &= \exp\left(-\frac{1}{2}\left(\frac{\sigma_z}{c}\omega\right)^2\right), \\ h(\omega) &= \exp\left(-\left(\frac{\sigma_z}{c}\omega\right)^2\right), \end{aligned} \tag{2}$$

are shown in Fig. 2 for positive frequencies. The RMS width of the functions $\widetilde{g}$ and h are $c/\sigma_z = 2\pi \cdot 636.1$ MHz and $c/(\sqrt{2}\,\sigma_z) = 2\pi \cdot 449.8$ MHz respectively. The interaction of the beam with the vacuum chamber can be characterized by an impedance $Z_{||}(\omega)$ and the power loss P of the beam is proportional to

$$P \sim \sum_{p=-\infty}^{p=+\infty} \Re[Z_{||}(p\,\omega_b)]h(p\,\omega_b), \tag{3}$$

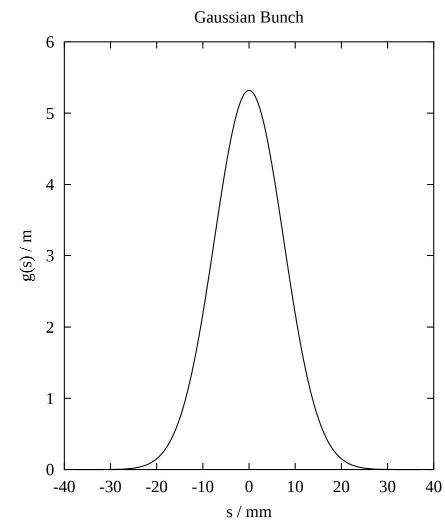

Figure 1: Gaussian bunch with an rms bunch length of $\sigma_z = 7.5$ cm.

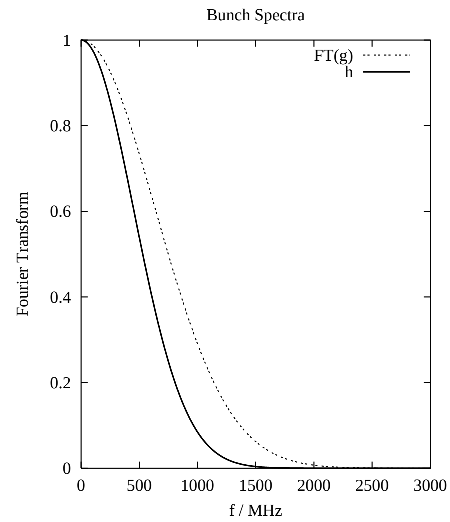

Figure 2: Fourier Transforms of the Gaussian bunch. The function $\widetilde{g}$ and h are plotted versus the frequency $\omega/(2\,\pi)$.

where $\omega_b/(2\,\pi) \approx 40\,\text{MHz}$ is the bunch repetition frequency [6]. From the plot of the function h (Fig. 2) it is obvious that it is sufficient to know the longitudinal impedance up to a frequency $\omega/(2\,\pi)$ of about 1.0 GHz to compute the power loss of the beam.

1.2 The CMS vacuum chamber

Inside of the CMS (Compact Muon Solenoid) experiment a vacuum chamber is installed which is accommodated to the needs of the installed detector components. A 3D-view of the vacuum system is shown in Fig. 3 and the dimensions of the main components are listed in Table 2.

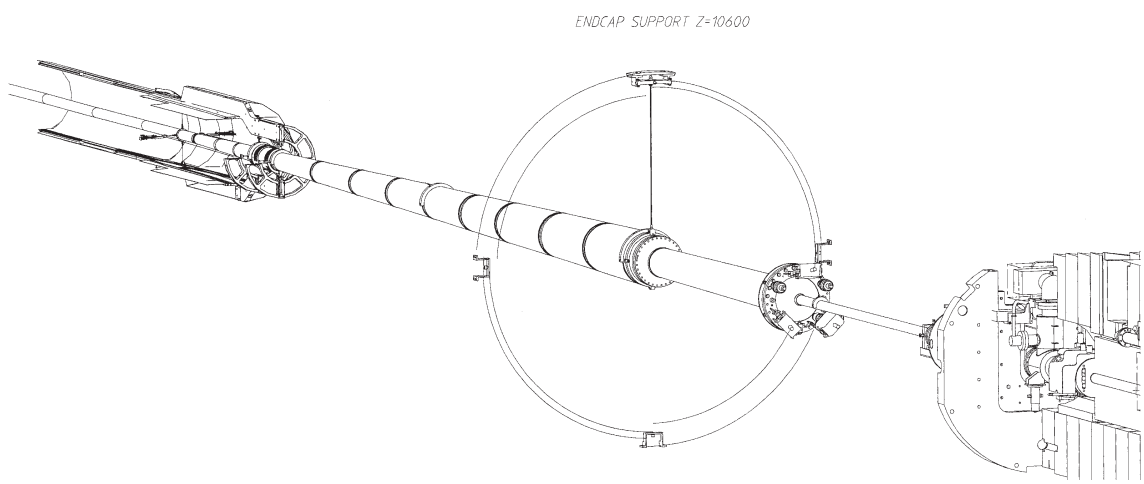

Figure 3: A 3D view of the CMS vacuum chamber. The beam pipe is shown from the interaction point to the compensation module.

Name		z / mm	r /mm	Material	Cu 0.1μm	RF-shield
CP	1	0.0	29.0	Be	no	
	2	1948.0	29.0	Be	no	**no**
	3	2353.6	34.9	Steel	no	
	4	2736.6	40.5	Steel	no	
	5	3120.0	46.1	Steel	no	
EC	6	3500.0	59.0	Steel	yes	
	7	4279.0	67.0	Steel	yes	
	8	5049.0	78.5	Steel	yes	
	9	5779.0	89.5	Steel	yes	
	10	6510.0	100.5	Steel	yes	
	11	7234.0	110.5	Steel	no	
	12	7959.0	122.0	Steel	no	
	13	8841.0	135.0	Steel	no	
	14	9723.0	148.0	Steel	no	
	15	10538.0	160.0	Steel	no	
	16	10715.0	110.7	Steel	no	
HF	17	10809.0	85.3	Steel	yes	
	18	13152.0	103.5	Steel	yes	
	19	13359.0	104.0	Steel	no	yes
CT2	20	13427.0	27.6	Steel	no	yes
	21	15870.0	27.6	Steel	yes	
	22	16070.0	27.6	Steel	yes	
CM	23	16380.0	31.5	Steel	no	yes
FP	24	16580.0	40.0	Steel	yes	
	25	18030.0	50.0	Steel	yes	
Pump	26	18500.0	50.0		no	yes
Bellow	27	18700.0	44.4		no	yes
Trans	28	19300.0	27.6		yes	

CP	=Central Pipe
EC	=End-cap Pipe
HF	=HF (Hadron forward) Pipe
CT2	=CT2 Pipe
CM	=Compensation Module
FP	=Forward Pipe
Pump	=Vacuum pump
Trans	=Transition Module

Table 2: The main components of the CMS vacuum system [7]. The longitudinal position z measured from the IP and the radial dimensions are listed as well as the material properties.

The beam pipe close to the interaction point (IP) is made from Beryllium (Be) while the other parts of the vacuum chamber are made from stainless steal. The vacuum chamber is coated with NEG (Non Evaporable Getter) material (TiZrV) [8] to absorb residual gas molecules and provide good vacuum conditions in the CMS beam pipe. The NEG material is in some regions covered with a thin (0.1μm thick) copper layer [7]. Along the beam pipe several bellows are installed. Most bellows are shielded against the beam induced rf-fields. At the transition between the Beryllium and the stainless steel parts of the central beam pipe the bellow is not shielded. The shape of the vacuum chamber based on the 28 data points from Table 2 is plotted in Fig. 4. The vacuum chamber has a rotational symmetry along the

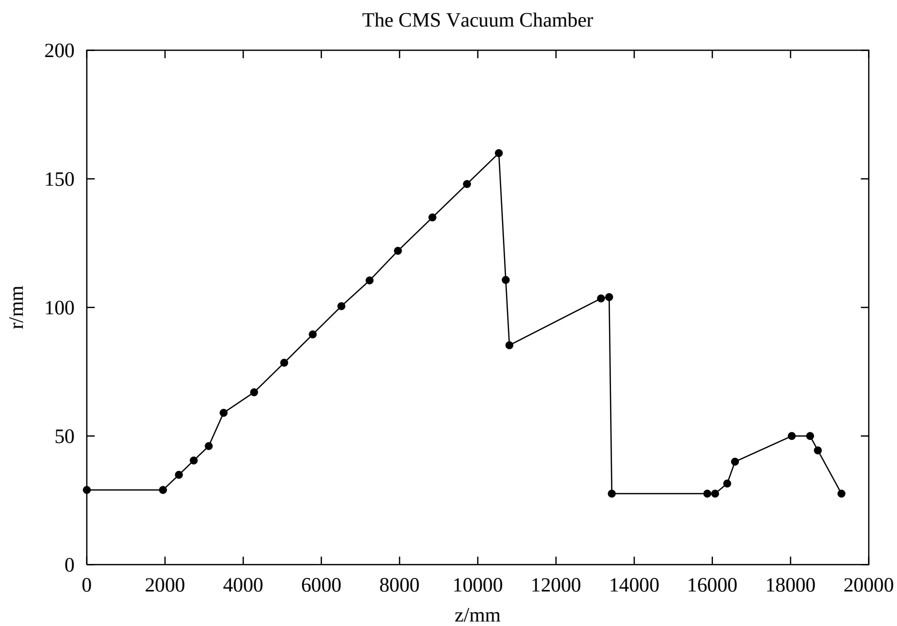

Figure 4: Schematic representation of the vacuum chamber of the CMS experiment at the LHC. The vacuum chamber has a rotational symmetry along the z axis. All dimensions are in mm. The interaction point (IP) is at $z = 0$ mm. The marked points correspond to the positions in Table 2.

z axis and is mirror symmetric with respect to the interaction point. In Fig. 5 the present (2008) and a previous version of the vacuum chamber from 1995 [2] is shown, which has been used for HOM calculations in [2, 3, 4]. Furthermore two tapered transitions (thin dashed lines) are show which have been suggested already in Ref. [2] to mitigate the wakefields in the CMS vacuum chamber. A comparison of the different versions of the vacuum chamber in Fig. 5 shows that the suggested tapers have been implemented in the present design, using admittedly a somewhat shorter taper length. The smaller radius (now 16 cm) is also an advantage of the present design since the spectrum of the HOMs is shifted to higher frequencies and therefore out of the bunch spectrum (see Fig. 2). Coherent excitation of HOMs and the associated losses have been first discussed in Ref. [4]. The installation of a special rf-screen in the End-Cap pipe, as suggested in [4], has not been implemented in the present design.

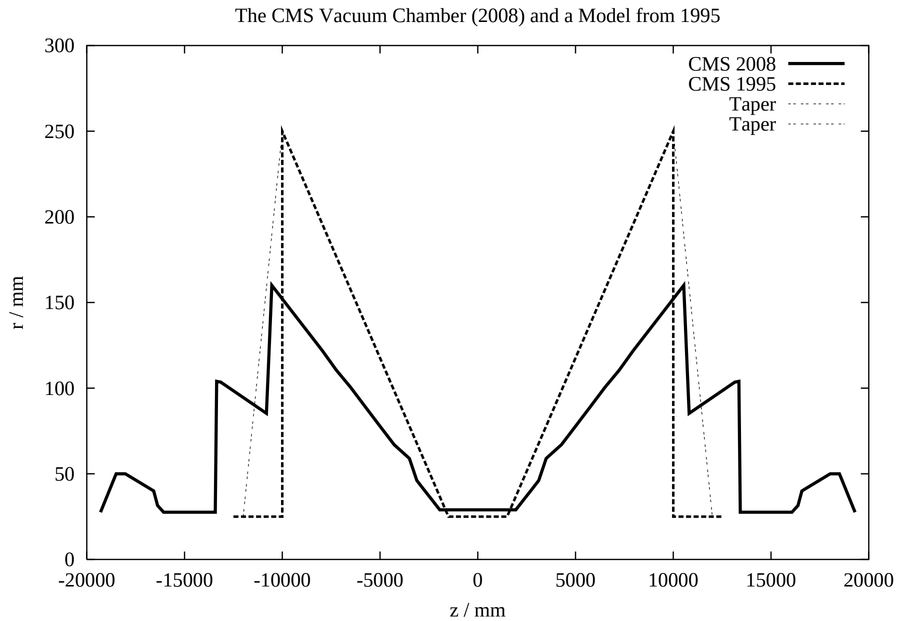

Figure 5: Schematic representation of the presently (2008) installed CMS vacuum chamber and a model of the CMS vacuum chamber from 1995, which was used for HOM calculations [2]. Furthermore some tapered transitions are show which were previously suggested in [2] to mitigate wakefield effects. All dimensions are in mm. The interaction point (IP) is at $z = 0$ mm.

1.3 Wakefields and HOMs

A beam circulating in a storage ring interacts with its vacuum chamber surroundings via electromagnetic fields. These wake fields [9] in turn act back on the beam and can lead to instabilities, which limit either the achievable current per bunch or the total current or even both. Transient and coherent losses may also heat the vacuum chamber which can be a problem by itself or may cause a degeneration of the vacuum conditions in the beam pipe. The long range wake potential can be represented as a sum over contributions from HOMs.

This report summarizes the properties of fifty monopole and dipole HOMs of the vacuum chamber of the CMS experiment with a frequency up to about 1.3 GHz. Field plots of several modes are provided to visualize the properties of the different types of modes. Extensive graphical representation of the HOMs can be found in the appendices. The study of the HOMs is complemented with a time domain calculation of the longitudinal monopole and the transverse dipole wake potential. The definitions of the rf-parameters of the modes which are used within this report are explained in the next section.

2 Definitions of RF-parameters

The purpose of this section is to provide the definitions of the rf-parameters including R/Q and G_1, which are used in the next sections. In particular, for dipole modes it is important to clarify the definitions used in this note since there exist no unified standard in the literature. First it is explained which parameters can be obtained from the eigenmodes calculated by the computer code MAFIA [10, 11]. Then it is explained how the parameters are related to long range wakefields.

2.1 Modes in a cavity

Consider any mode in a cavity with the frequency $f = \omega/(2\,\pi)$. One obtains in complex notation for the electric and magnetic field:

$$\begin{aligned} \boldsymbol{E}(r,\phi,z,t) &= \widetilde{\boldsymbol{E}}(r,\phi,z)\,\exp(-i\,\omega\,t) \\ \boldsymbol{B}(r,\phi,z,t) &= \widetilde{\boldsymbol{B}}(r,\phi,z)\,\exp(-i\,\omega\,t). \end{aligned} \tag{4}$$

Generally the fields $\widetilde{\boldsymbol{E}}(r,\phi,z)$ and $\widetilde{\boldsymbol{B}}(r,\phi,z)$ in geometries with cylindrical symmetry can be written as (in a multi-pole expansion) [12] :

$$\begin{aligned} \widetilde{\boldsymbol{E}}(r,\phi,z) &= \sum_m \Big(\widetilde{E_r^{(m)}}(r,z)\,\cos(m\,\phi)\;\;\boldsymbol{e_r} \\ &\qquad + \widetilde{E_\phi^{(m)}}(r,z)\,\sin(m\,\phi)\;\;\boldsymbol{e_\phi} \\ &\qquad + \widetilde{E_z^{(m)}}(r,z)\,\cos(m\,\phi)\;\;\boldsymbol{e_z} \Big) \\ \widetilde{\boldsymbol{B}}(r,\phi,z) &= \sum_m \Big(\widetilde{B_r^{(m)}}(r,z)\,\sin(m\,\phi)\;\;\boldsymbol{e_r} \\ &\qquad + \widetilde{B_\phi^{(m)}}(r,z)\,\cos(m\,\phi)\;\;\boldsymbol{e_\phi} \\ &\qquad + \widetilde{B_z^{(m)}}(r,z)\,\sin(m\,\phi)\;\;\boldsymbol{e_z} \Big). \end{aligned} \tag{5}$$

For the CMS experimental vacuum chamber the computer code MAFIA [10, 11] has been used to calculate the field components $\widetilde{E_r^{(m)}}$, $\widetilde{E_\phi^{(m)}}$, etc. The results are presented in the next sections for $m = 0$ and 1 (the monopole, dipole modes).

In the plane $\phi = 0$ only longitudinal and radial electric field and azimuthal magnetic field components are present:

$$\begin{aligned} \widetilde{\boldsymbol{E}}(r,0,z) &= \sum_m \Big(\widetilde{E_r^{(m)}}(r,z)\;\;\boldsymbol{e_r} \\ &\qquad + \widetilde{E_z^{(m)}}(r,z)\;\;\boldsymbol{e_z} \Big) \\ \widetilde{\boldsymbol{B}}(r,0,z) &= \sum_m \Big(\widetilde{B_\phi^{(m)}}(r,z)\;\;\boldsymbol{e_\phi} \Big). \end{aligned} \tag{6}$$

The magnetic field can be calculated from the electric field according to the Maxwell equation:

$$\boldsymbol{\nabla} \times \widetilde{\boldsymbol{E}}(r,\phi,z) = i\,\omega\,\widetilde{\boldsymbol{B}}(r,\phi,z).$$

The azimuthal magnetic field component is given simply by:

$$\widetilde{B_\phi^{(m)}}(r,z) = \frac{-i}{\omega}\left(\frac{\partial}{\partial z}\widetilde{E_r^{(m)}}(r,z) - \frac{\partial}{\partial r}\widetilde{E_z^{(m)}}(r,z)\right). \tag{7}$$

The azimuthal component of the electric field is also related to the radial and longitudinal components of the electric field since the Maxwell equation $\boldsymbol{\nabla} \cdot \widetilde{\boldsymbol{E}}(r,\phi,z) = 0$ holds for all modes. For $m = 0$ the azimuthal component of the electric field is identical to zero, while for $m > 0$ one obtains:

$$\widetilde{E_\phi^{(m)}}(r,z) = -\frac{1}{m}\left[\widetilde{E_r^{(m)}}(r,z) + r\ \left(\frac{\partial}{\partial r}\widetilde{E_r^{(m)}}(r,z) + \frac{\partial}{\partial z}\widetilde{E_z^{(m)}}(r,z)\right)\right]. \tag{8}$$

Therefore it is sufficient to know the electric field in the plane $\phi = 0$, i.e. once the components $\widetilde{E_r^{(m)}}(r,z)$ and $\widetilde{E_z^{(m)}}(r,z)$ are known it is possible to reconstruct the complete electric and magnetic field pattern of the considered mode. The next sections contain some Figures which show arrow-plots of the electric field always in the plane $\phi = 0$. These plots contain the complete information of the electric and magnetic field of the mode since all other field components provide only redundant information. But mainly plots of the longitudinal field component $\widetilde{E_z^{(m)}}(r_0,z)$ for a fixed radius $r = r_0$ as a function of z are shown since this quantity enters into the loss parameter and R/Q (see the next subsection).

2.1.1 The loss parameter and R/Q

The interaction of the beam with a cavity mode is characterized by the loss parameter $k_\parallel^{(m)}$ or by the quantity R/Q [9][1]. These parameters can be determined from the numerically calculated fields using the MAFIA post-processor [10, 11]. The longitudinal voltage at a fixed radius r is defined as

$$V_\parallel^{(m)}(r) = \int_0^L dz\,\widetilde{E_z^{(m)}}(r,z)\exp(-i\,\omega\,z/c), \tag{9}$$

while the total stored energy of the considered mode is given by:

$$U^{(m)} = \frac{\epsilon_0}{2}\ \int d^3r\ \left|\widetilde{\boldsymbol{E^{(m)}}}\right|^2. \tag{10}$$

From the voltage and stored energy the loss parameter and R/Q can be calculated:

$$\begin{aligned} k^{(m)}(r) &= \frac{\left|V_\parallel^{(m)}(r)\right|^2}{4\,U^{(m)}} \\ \frac{R^{(m)}}{Q} &= \frac{1}{r^{2\,m}}\frac{2\ k^{(m)}(r)}{\omega}. \end{aligned} \tag{11}$$

[1]The definition of the shunt impedance $R = Q\,(R/Q)$ here is $V^2/(2\,P)$. If one multiplies (R/Q) by a factor of two one obtains values which are in agreement with the "linac" definition V^2/P for the shunt impedance.

For monopole modes the superscript (0) is usually omitted $R/Q = R^{(0)}/Q$. $R^{(m)}/Q$ is independent of the radius r since it can be shown (see [9, 13]) that $V^{(m)}(r) \sim r^m$ and therefore $k^{(m)}(r) \sim r^{2m}$. For dipole modes one obtains:

$$\frac{R^{(1)}}{Q} = \frac{1}{r^2}\frac{2\,k^{(1)}(r)}{\omega}. \tag{12}$$

$R^{(1)}/Q$ is measured in Ohm/m^2.

2.1.2 The geometry parameter G_1 and the Q-value

The power P_{sur} dissipated into the cavity wall due to the surface resistivity R_{sur} can be calculated from the tangential magnetic field:

$$P_{sur} = \frac{1}{2}\,R_{sur}\,\int dA\,|H_\phi|^2\,. \tag{13}$$

The power dissipated into the cavity surface can also be characterized by the quality factor Q_0 or the geometry parameter G_1 [15], which are defined as:

$$Q_0 = \frac{\omega\,U}{P_{sur}} \tag{14}$$

$$G_1 = R_{sur}\,Q_0, \tag{15}$$

where U is the total field energy and $\omega = 2\pi\,f$ is the frequency of the mode. G_1 is a purely geometric quantity which is independent of the cavity material. Therefore G_1 will be quoted throughout this report for the different cavity modes.

In the MAFIA post-processor the dissipated power P_{sur} is calculated by default for a copper cavity with the surface resistivity:

$$R_{Cu} = \sqrt{\frac{\omega\,\mu_0}{2\,\sigma_{Cu}}}, \qquad \sigma_{Cu} = 5.8\cdot 10^7\ (\Omega\,\mathrm{m})^{-1}. \tag{16}$$

From the quality factor for copper and R_{Cu} the parameter G_1 can be obtained.

In general the total damping of a mode is not only determined by the surface losses but also by coupling to external waveguides (HOM-couplers). Therefore one has to distinguish the Q-value Q_0 which is defined above and the external Q-value Q_{ext} which characterizes the coupling to external waveguides. For the vacuum chamber of the CMS experiment no HOM-couplers are foreseen.

2.2 TM- and TE-modes in circular waveguides

In this subsection the properties of the modes which can propagate in a simple circular waveguide [14] are summarized. In general one can distinguish TM- and TE-modes, which are characterized by the properties of the electric and magnetic field components.

For **TM-modes** the longitudinal magnetic field vanishes everywhere, and the longitudinal electric field is a solution of the differential equation:

$$\left[\boldsymbol{\nabla}_\perp{}^2 + \left(\left(\frac{\omega}{c}\right)^2 - k_z{}^2\right)\right] E_z = 0, \qquad B_z \equiv 0. \tag{17}$$

In the case of a circular waveguide (beam pipe) the solution is

$$E_z \sim J_m(j_{n,m}\, r/r_0)\, \exp(i\, m\, \phi), \tag{18}$$

where $j_{n,m}$ is the n-th zero of the Bessel-function J_m, and r_0 is the radius of the beam pipe. This solution is required by the boundary condition $E_z(r_0) = 0$ at the inner surface of the pipe. The mode is called a $\mathrm{TM}_{m,n}$ mode. All transverse fields are determined by the longitudinal fields:

$$\boldsymbol{E}_\perp = i\, \frac{k_z}{\sqrt{(\omega/c)^2 - k_z{}^2}}\, \boldsymbol{\nabla}_\perp E_z, \qquad \boldsymbol{B}_\perp = \frac{1}{c}\, \frac{\omega/c}{k_z}\, \boldsymbol{e_z} \times \boldsymbol{E}_\perp, \tag{19}$$

with e_z the unit vector in the z-direction. From equations (17) and (18) the following dispersion relation is obtained:

$$f = \frac{c}{2\,\pi} \sqrt{\left(\frac{j_{n,m}}{r_0}\right)^2 + k_z{}^2}, \tag{20}$$

where k_z is the propagation constant in the longitudinal direction. Only modes with frequencies f above the cutoff frequency

$$f_{cTM} = c\, \frac{j_{n,m}}{2\,\pi}\, \frac{1}{r_0} \tag{21}$$

can propagate in the beam pipe (i.e. real k_z).

For **TE-modes** the longitudinal electric field vanishes everywhere, and the longitudinal magnetic field is a solution of the differential equation:

$$\left[\boldsymbol{\nabla}_\perp{}^2 + \left(\left(\frac{\omega}{c}\right)^2 - k_z{}^2\right)\right] B_z = 0, \qquad E_z \equiv 0. \tag{22}$$

The transverse fields are determined by the longitudinal fields:

$$\boldsymbol{B}_\perp = i\, \frac{k_z}{\sqrt{(\omega/c)^2 - k_z{}^2}}\, \boldsymbol{\nabla}_\perp B_z, \qquad \boldsymbol{E}_\perp = c\, \frac{\omega/c}{k_z}\, \boldsymbol{B}_\perp \times \boldsymbol{e_z}. \tag{23}$$

In the case of a circular waveguide (beam pipe) the solution of equation (22) must fulfill the boundary condition B_r=0 or $\partial B_z/\partial r = 0$ at the inner surface of the pipe. The following solution

$$B_z \sim J_m(j'_{n,m}\, r/r_0)\, \exp(i\, m\, \phi), \tag{24}$$

meets the requirement where $j'_{n,m}$ is the n-th zero of the derivative of the m-th Bessel-function. The mode is called a TE$_{m,n}$ mode. The derivatives of the Bessel-functions can be written in terms of Bessel-functions. For $m = 0, 1$, and 2 one obtains:

$$\begin{aligned} \frac{d}{dx} J_0(x) &= -J_1(x) \\ \frac{d}{dx} J_1(x) &= J_0(x) - \frac{1}{x}\, J_1(x) \\ \frac{d}{dx} J_2(x) &= J_1(x) - \frac{2}{x}\, J_2(x). \end{aligned} \tag{25}$$

From equations (22) and (24) the following dispersion relation is obtained:

$$f = \frac{c}{2\,\pi} \sqrt{\left(\frac{j'_{n,m}}{r_0}\right)^2 + {k_z}^2}. \tag{26}$$

The cutoff frequency for TE-modes is:

$$f_{cTE} = c\, \frac{j'_{n,m}}{2\,\pi}\, \frac{1}{r_0}. \tag{27}$$

The first four zeros of the Bessel-functions and their derivatives of order $m = 0, 1$, and 2 multiplied by the factor $c/(2\,\pi)$ are listed in Table 3. The cutoff frequencies for the TM- and TE-modes are listed in Table 4 for a circular wave guide with a radius of 29 mm corresponding to the radius of the CMS vacuum chamber in the IP region.

	$c\, j_{n,m}/(2\,\pi)$ / (GHz cm)			$c\, j'_{n,m}/(2\,\pi)$ / (GHz cm)		
n	m=0	m=1	m=2	m=0	m=1	m=2
1	11.4743	0	0	0	8.7849	0
2	26.3382	18.2824	24.5038	18.2824	25.4382	14.5728
3	41.2899	33.4738	40.1616	33.4738	40.7297	31.9973
4	56.2615	48.5411	55.4423	48.5411	55.8534	47.5678

Table 3: Zeros of Bessel-functions and their derivatives multiplied by the factor $c/(2\,\pi)$.

	f_{cTM} / GHz			f_{cTE} / GHz		
n	m=0	m=1	m=2	m=0	m=1	m=2
1	3.9567	0	0	0	3.0293	0
2	9.0821	6.3043	8.4496	6.3043	8.7718	5.0251

Table 4: Cutoff frequencies for TM- and TE-modes in a circular waveguide with a radius of 29 mm.

2.3 Wakefields

Consider the situation shown in Fig. 6. A test charge q_2 follows a point charge q_1 at a distance s. It is assumed that both charges are relativistic ($v \approx c$). The Lorentz force on the test charge due to the fields generated by the point charge q_1 is

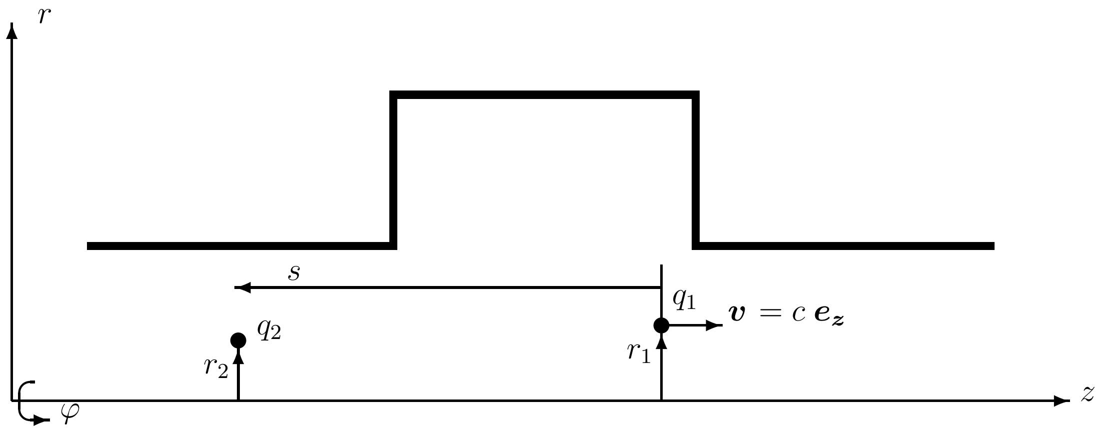

Figure 6: A point charge q_1 traversing a cavity with an offset r_1 followed by a test charge q_2 with offset r_2 .

$$\boldsymbol{F} = \frac{d\boldsymbol{p}}{dt} = \; q_2\,(\boldsymbol{E} + c\,\boldsymbol{e_z} \times \boldsymbol{B}). \tag{28}$$

The **wake potential** of the point charge q_1 is defined as:

$$\boldsymbol{W}\,(x_2, y_2, x_1, y_1, s) = \frac{1}{q_1} \int_0^L dz(\boldsymbol{E} + c\,\boldsymbol{e_z} \times \boldsymbol{B})_{t=(z+s)/c}. \tag{29}$$

The wake potential may be regarded as an average of the Lorentz force on a test charge. Causality requires $\boldsymbol{W}\,(s) = 0$ for $s < 0$. The distance s is positive in the direction opposite to the motion of the point charge q_1.

The longitudinal and transverse components of the wake potential are connected by the Panofsky–Wenzel theorem [16]

$$\frac{\partial}{\partial s}\boldsymbol{W}_{\perp}(x_2, y_2, x_1, y_1, s) = -\boldsymbol{\nabla}_{\perp_2} W_{\|}(x_2, y_2, x_1, y_1, s). \tag{30}$$

Integration of the transverse gradient (applied to the transverse coordinates of the test charge) of the longitudinal wake potential yields the transverse wake potential.

2.3.1 Multipole expansion of the wake potential

If the structure traversed by the bunch is cylindrically symmetric then a multipole expansion can be used to describe the wake potential. Consider again the situation shown in Fig. 6. Assume that the point charge q_1 traverses the cavity at position (r_1, φ_1), while the test charge follows at position (r_2, φ_2). The longitudinal wake potential is given by:

$$W_{\|}(r_1, r_2, \varphi_1, \varphi_2, s) = \sum_{m=0}^{\infty} {r_1}^m\, {r_2}^m\; W_{\|}^{(m)}(s)\;\; \cos m\,(\varphi_2 - \varphi_1). \tag{31}$$

There is no a priori relation between the wake potentials of different azimuthal order m. The functions $W_{\|}^{(m)}(s)$ are the longitudinal m-pole wake potentials. It is often sufficient to consider only the leading terms of the series in equation (31), neglecting contributions from quadrupole and higher multipole components. In Cartesian coordinates the longitudinal wake potential is approximately:

$$\begin{aligned} W_{\|}(x_1, y_1, x_2, y_2, s) \;\approx\; & W_{\|}^{(0)}(s) \\ & + (x_2\; x_1 + y_2\; y_1)\; W_{\|}^{(1)}(s). \end{aligned} \tag{32}$$

The transverse wake potential can be calculated using the Panofsky–Wenzel theorem:

$$\boldsymbol{W}_{\perp}(x_1, y_1, x_2, y_2, s) \approx (x_1\; \boldsymbol{e_x} + y_1\; \boldsymbol{e_y})\; W_{\|}^{(1)}(s). \tag{33}$$

The transverse m-pole wake potentials are defined as:

$$W_{\perp}^{(m)}(s) = -\int_{-\infty}^{s} ds'\, W_{\|}^{(m)}(s'), \tag{34}$$

for $m > 0$. There is no transverse monopole wake potential. The dipole wake potential does not depend on the position of the test charge q_2. The kick on the test charge is linear in the offset of the point charge q_1.

2.3.2 Wakefields due to HOMs

If only the long range wake fields are considered then it is possible to calculate the m-pole wake potentials $W_{\|}^{(m)}(s)$ as a sum over all modes [9]. The longitudinal m-pole wake potential is:

$$W_{\|}^{(m)}(s) = -\sum_n\; 2\,\frac{1}{a^{2\,m}}\, k_{\| n}^{(m)}(a)\cos(\omega_n\, s/c), \qquad s > 0, \tag{35}$$

where ω_n are the frequencies of the m-pole modes, and $k_{\| n}^{(m)}(a)$ are the loss parameters. The transverse m-pole wake potential ($m > 1$) according to equations (35) and (34) is:

$$W_{\perp}^{(m)}(s) = \sum_n\; 2\,\frac{k_{\| n}^{(m)}(a)}{\omega_n\, a^{2m}/c}\; \sin(\omega_n\, s/c), \qquad s > 0. \tag{36}$$

For dipole modes it is common to define a kick parameter $k_{\perp n}$:

$$k_{\perp n} = \frac{k_{\| n}^{(1)}(a)}{\omega_n\, a^2/c}. \tag{37}$$

It is possible to rewrite the above equations in terms of $R^{(m)}/Q$:

$$\begin{aligned} W_{\|}^{(m)}(s) \;&=\; -\sum_n\; \omega_n \left(\frac{R^{(m)}}{Q}\right)_n \cos(\omega_n\, s/c)\;\; \exp(-1/\tau_n\;\, s/c) \\ W_{\perp}^{(m)}(s) \;&=\; c\sum_n\; \left(\frac{R^{(m)}}{Q}\right)_n \sin(\omega_n\, s/c)\;\; \exp(-1/\tau_n\;\, s/c). \end{aligned} \tag{38}$$

A damping term has been included with the damping time τ_n for mode n. If wall losses dominate the damping of the fields the damping time is:

$$\tau_n \approx \frac{2\,(Q_0)_n}{\omega_n}. \tag{39}$$

3 Higher Order Modes - HOMs

The computer code MAFIA [10, 11] has been used to calculate the electric and magnetic fields in the frequency domain. A 2-dimensional model of the CMS vacuum chamber has been used since it is sufficient to model a cylindrically symmetric structure on a $r-z$-grid to obtain all important rf-parameters. The details of the geometric model are listed in Table 5 and are plotted in Fig. 7. For the calculation a mesh with a step size of 1 mm in the radial (r) and 2 mm in the longitudinal (z) direction with a total number of $161 \times 8036 = 1293796$ grid points has been used. Electric (E) boundary conditions were used at both ends of the modeled structure. The MAFIA eigenvalue solver was used to calculate 50 monopole modes and also 50 dipole modes. The modes are labeled as "EE-n" according to the boundary conditions at both ends and the mode number n, starting with the label "EE-1" for the mode with the lowest frequency.

Name		z / mm	r /mm	Material	Cu	RF-shield
CP	1	0	29.0	Be	no	no
	2	1948	29.0	Be	no	no
EC	3	10538	160.0	Steel	no	
HF	4	10809	85.3	Steel	yes	
	5	13359	104.0	Steel	no	yes
CT2	6	13427	27.6	Steel	no	yes
	7	16070	27.6	Steel	yes	

Table 5: The MAFIA model of the CMS vacuum chamber.

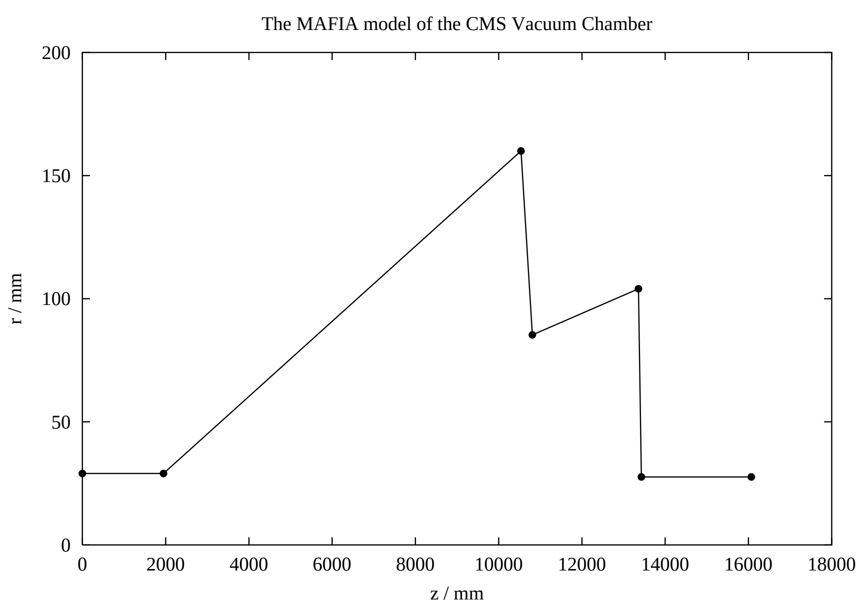

Figure 7: Schematic representation of the MAFIA model of the CMS vacuum chamber. All dimensions are in mm. The interaction point (IP) is at $z = 0$ mm. The marked points correspond to the positions in Table 5.

From the electric and magnetic fields the loss parameter, R/Q, G_1 and Q-value were obtained according to the definitions in section 2. The Q-value of a mode can be calculated from the conductivity of the material and the parameter G_1:

$$Q_{Mat} = \frac{G_1}{R_{sur}} = G_1\, \sigma_{Mat}\, \delta_{skin}, \tag{40}$$

where σ_{Mat} is the conductivity of the material, R_{sur} the surface resistance, and δ_{skin} the skin depth:

$$R_{sur} = \sqrt{\frac{\omega\ \mu_0}{2\ \sigma_{Mat}}}, \qquad \delta_{skin} = \sqrt{\frac{2}{\omega\, \mu_0\, \sigma_{Mat}}}. \tag{41}$$

The Q-values for copper (Cu) can be scaled to the Q-value of another material:

$$Q_{Mat} = \sqrt{\frac{\sigma_{Mat}}{\sigma_{Cu}}} Q_{Cu}. \tag{42}$$

The conductivities for copper, steel and NEG [17, 18] and the corresponding skin depths for an rf-frequency of 1 GHz are listed in Table 6. Since the thickness of the NEG layer (about 1 μm) and the copper coating (about 0.1 μm) is much thinner than the skin depth at a typical mode frequency of 1 GHz the Q-value will be dominated by the material of the vacuum chamber which is stainless steel in all regions were HOMs are trapped inside the CMS vacuum chamber. The Q-value of all modes is therefore about 16 % of the Q-value at which a mode in a copper chamber would ring. In the next two subsections the results

Material	σ_{Mat} / $(\Omega\,\mathrm{m})^{-1}$	δ_{skin} /(μm) (f = 1 GHz)
Copper	$58 \cdot 10^6$	2.1
Steel	$1.5 \cdot 10^6$	12.9
NEG	$0.31 \cdot 10^6$	28.5

Table 6: Conductivity of several materials and the corresponding skin depth at a frequency of 1 GHz.

for the monopole and dipole modes are listed in tables (see Tab. 7, 8, 9 and 10) and are complemented with a few plots of the electric fields. Plots of the longitudinal electric field for *all* modes can be found in Appendix A and B for the monopole modes and for the dipole modes respectively.

3.1 Monopole Modes

In general one has to distinguish between TM- and TE-monopole modes. But the beam can only interact with TM-modes since the longitudinal electric field is identical to zero for TE-modes, i.e. the loss parameter is identically zero for TE-modes. Therefore only TM-monopole modes are considered in this subsection. The monopole mode with the lowest frequency of 751.0 MHz (EE-1) is trapped at the end of the End-cap-pipe about 10 m from the interaction point. The electric field of that mode is shown in Fig. 8, while the electric field of mode EE-2 (f = 786.6 MHz) is plotted in Fig. 9 also in the region between 9 m to

11 m from the IP. The MAFIA model of the CMS vacuum chamber is plotted together with the longitudinal electric field of mode EE-1 and EE-2 in Fig. 10 and Fig. 11. This clearly shows where the modes are trapped inside the vacuum chamber.

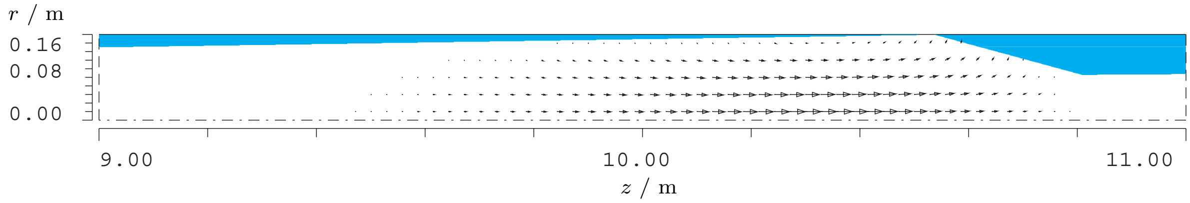

Figure 8: Electric field of mode EE-1 in the CMS vacuum chamber.

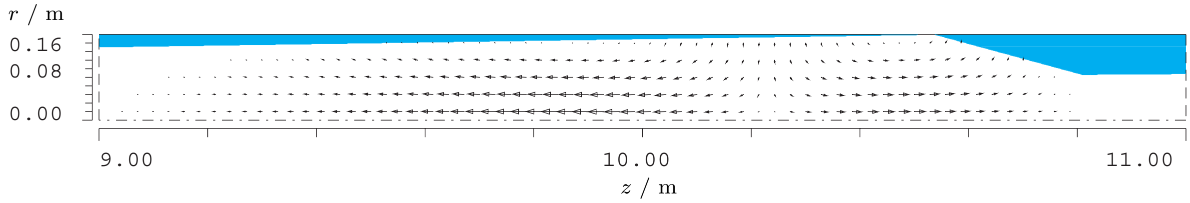

Figure 9: Electric field of mode EE-2 in the CMS vacuum chamber.

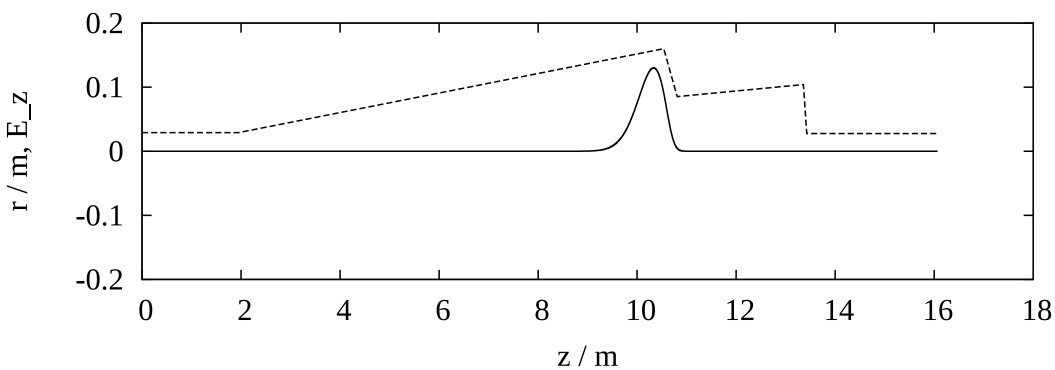

Figure 10: Longitudinal electric field (at $r = 0$ cm) of mode EE-1 in the CMS vacuum chamber.

The loss parameters of all 50 TM-monopole modes are plotted versus frequency in Fig. 12. The mode EE-19 ($f = 1137.7$ MHz) has the largest loss parameter of all calculated modes (3.123 V/nC). This mode is trapped in the HF part of the CMS vacuum chamber about 13 m from the IP. The electric field of that mode is plotted in Fig. 13. The MAFIA model of the CMS vacuum chamber is plotted together the longitudinal electric field of mode EE-19 in Fig. 14. The basic rf-parameters of all modes are summarized in Tables 7 and 8. Plots of the longitudinal electric fields of all 50 modes are shown in appendix A.

The numerical solution of the eigenvalue problem with the MAFIA code requires an estimate of the frequency of the highest searched eigenvalue (i.e. for mode EE-50). As a start an estimate of 2.5 GHz was chosen. The calculation has been repeated with an estimate of 1.6 GHz. The loss parameters for both runs are plotted in Fig. 15. The loss parameters for modes EE-1 to EE-41 are almost identical for both calculations while the data for modes

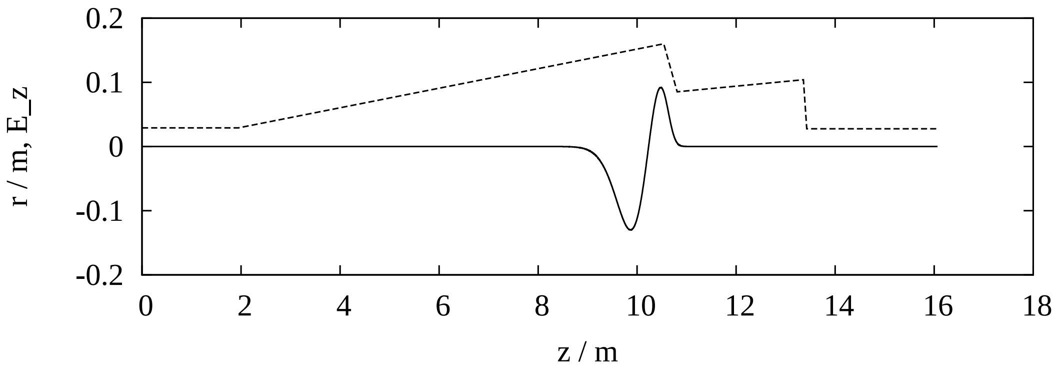

Figure 11: Longitudinal electric field (at $r = 0$ cm) of mode EE-2 in the CMS vacuum chamber.

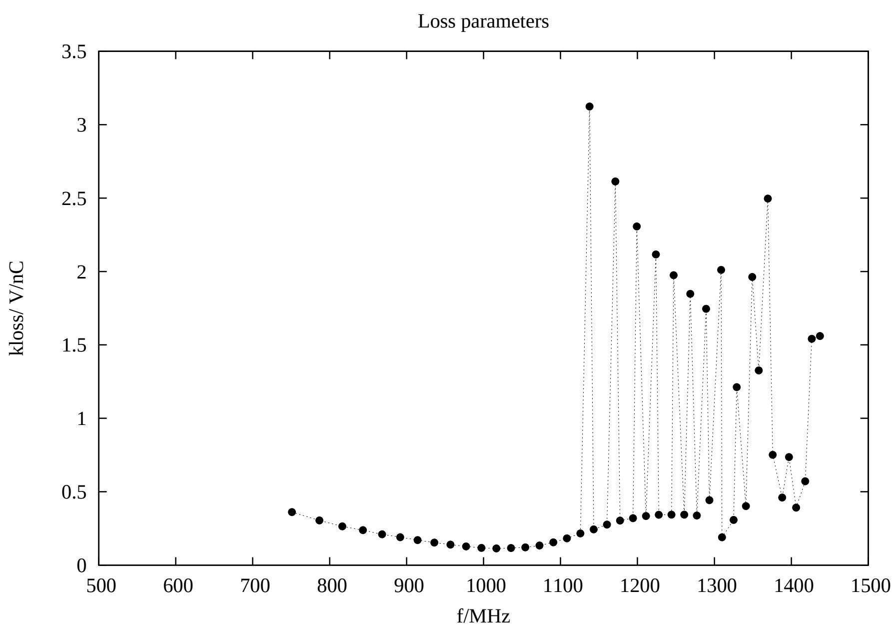

Figure 12: Plot of the loss parameters of the monopole modes versus frequency using the data from Tables 7 and 8. (The dotted line is intended only to guide the eye.)

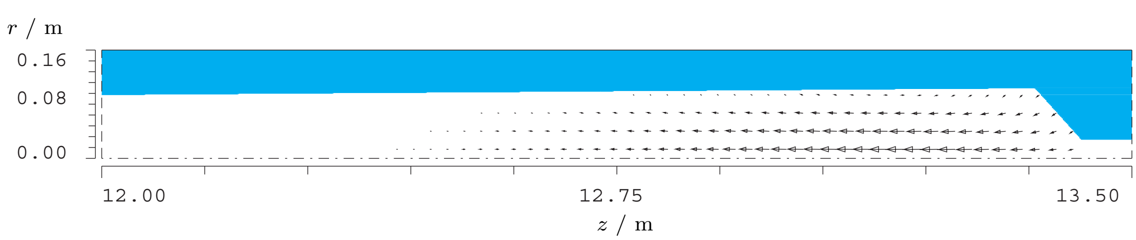

Figure 13: Electric field of mode EE-19 in the CMS vacuum chamber.

EE-42 to EE-50 depend strongly on the estimated frequency. The results presented in the tables 7 and 8 and Fig. 12 were obtained with an estimate of 1.6 GHz. This data set was chosen since the numerical error is smaller than for the data with an estimate of 2.5 GHz.

In the next subsection the results for the dipole modes are discussed before the transient and resonant losses due to monopole modes are discussed in a separated subsection.

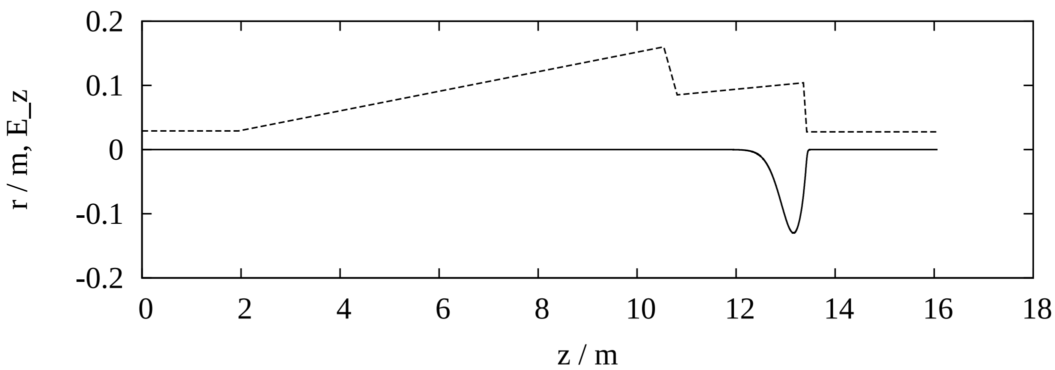

Figure 14: Longitudinal electric field (at $r = 0$ cm) of mode EE-19 in the CMS vacuum chamber.

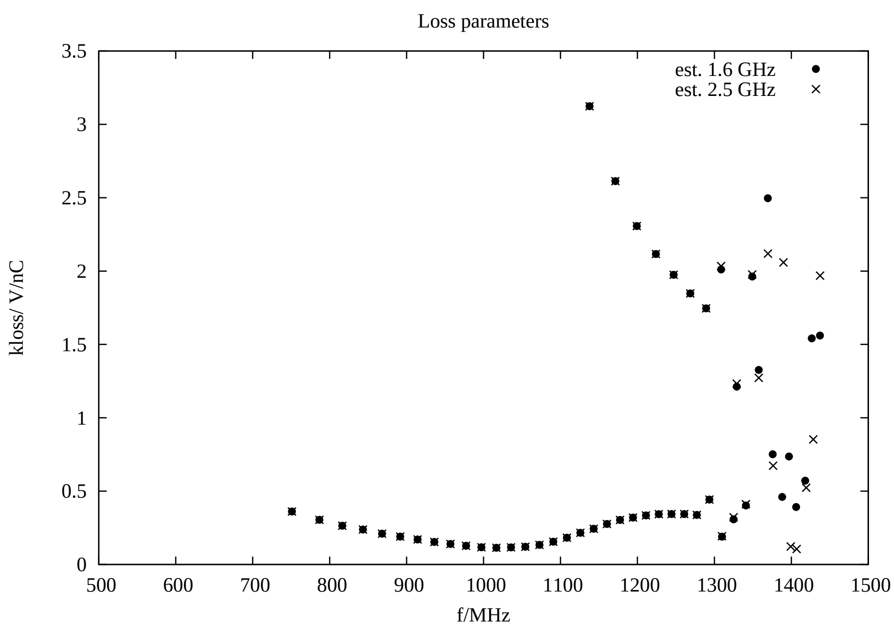

Figure 15: Plot of the loss parameters of the monopole modes versus frequency for two different estimates of the highest searched eigenvalue. The dots indicate the data set shown in Fig. 12.

Mode	f / MHz	$k^{(0)}$ /(V/nC)	G_1 / Ohm	R/Q / Ohm	Q_{Cu}	Q_{Steel}
EE- 1	751.0	0.361	450.3	0.153	63000	10080
EE- 2	786.6	0.305	458.5	0.123	62700	10030
EE- 3	816.4	0.264	465.2	0.103	62400	9980
EE- 4	843.3	0.238	471.1	0.090	62200	9950
EE- 5	868.2	0.210	476.5	0.077	62000	9920
EE- 6	891.8	0.190	481.5	0.068	61800	9890
EE- 7	914.3	0.171	486.3	0.059	61600	9860
EE- 8	936.0	0.154	490.9	0.052	61500	9840
EE- 9	956.9	0.140	495.3	0.046	61400	9820
EE-10	977.3	0.128	499.5	0.042	61200	9800
EE-11	997.2	0.117	503.7	0.037	61100	9780
EE-12	1016.6	0.114	507.5	0.036	61000	9760
EE-13	1035.6	0.116	511.4	0.036	60900	9750
EE-14	1054.3	0.121	514.9	0.037	60800	9720
EE-15	1072.6	0.134	518.5	0.040	60700	9710
EE-16	1090.6	0.155	521.8	0.045	60600	9690
EE-17	1108.3	0.183	525.0	0.053	60400	9670
EE-18	1125.8	0.216	528.4	0.061	60400	9660
EE-19	1137.7	3.123	441.0	0.874	50100	8020
EE-20	1143.2	0.243	531.2	0.068	60200	9640
EE-21	1160.3	0.276	534.4	0.076	60100	9620
EE-22	1171.3	2.613	447.5	0.710	50100	8020
EE-23	1177.3	0.304	537.6	0.082	60100	9610
EE-24	1194.2	0.320	540.5	0.085	60000	9590
EE-25	1199.2	2.307	452.3	0.612	50100	8010

Table 7: Monopole modes of the CMS vacuum chamber.

Mode	f / MHz	$k^{(0)}$ /(V/nC)	G_1 / Ohm	R/Q / Ohm	Q_{Cu}	Q_{Steel}
EE-25	1199.2	2.307	452.3	0.612	50100	8010
EE-26	1211.0	0.335	543.7	0.088	59900	9580
EE-27	1224.0	2.117	456.4	0.550	50000	8000
EE-28	1227.7	0.343	547.2	0.089	59900	9580
EE-29	1244.3	0.344	549.9	0.088	59800	9560
EE-30	1247.1	1.974	460.0	0.504	49900	7990
EE-31	1260.8	0.344	553.1	0.087	59700	9550
EE-32	1268.7	1.848	463.3	0.464	49900	7980
EE-33	1277.2	0.338	556.2	0.084	59700	9540
EE-34	1289.3	1.746	466.4	0.431	49800	7970
EE-35	1293.5	0.442	558.7	0.109	59500	9530
EE-36	1308.7	2.010	493.2	0.489	52300	8360
EE-37	1309.9	0.189	531.0	0.046	56200	9000
EE-38	1325.0	0.308	548.9	0.074	57800	9250
EE-39	1329.1	1.213	486.6	0.290	51200	8180
EE-40	1341.0	0.402	556.7	0.095	58300	9320
EE-41	1349.2	1.963	495.4	0.463	51700	8270
EE-42	1357.6	1.326	558.7	0.311	58100	9300
EE-43	1369.4	2.497	523.9	0.580	54300	8680
EE-44	1375.8	0.752	541.7	0.174	56000	8960
EE-45	1388.0	0.460	556.8	0.106	57300	9170
EE-46	1396.9	0.736	530.2	0.168	54400	8700
EE-47	1406.2	0.392	562.2	0.089	57500	9200
EE-48	1418.0	0.572	554.9	0.128	56500	9040
EE-49	1426.5	1.542	549.0	0.344	55700	8910
EE-50	1437.1	1.560	570.1	0.346	57600	9220

Table 8: Monopole modes of the CMS vacuum chamber.

3.2 Dipole Modes

The beam only interacts with dipole modes in the case that the beam traverses the CMS vacuum chamber off axis since the longitudinal electric field of any dipole mode vanishes on axis. The loss parameters of up to 75 dipole modes have been calculated for an offset of 1 cm from the axis of the vacuum chamber. From the loss parameters the transverse impedance has been obtained using the following relation:

$$Z_{\perp} = \frac{1}{\omega/c} \frac{R^{(1)}}{Q} Q_{Steel}, \tag{43}$$

and the Q-value for steel. A summary of the data of the dipole modes are given in tables 9 and 10.

The dipole mode with the lowest frequency of 584.0 MHz (EE-1) is trapped at the end of the End-cap-pipe about 10 m from the interaction point. The electric field is shown in Fig. 16. The mode EE-16 with a frequency of 882.5 MHz is trapped in the HF-pipe (see Fig. 17). The loss parameters of the dipole modes are plotted versus frequency in Fig. 18

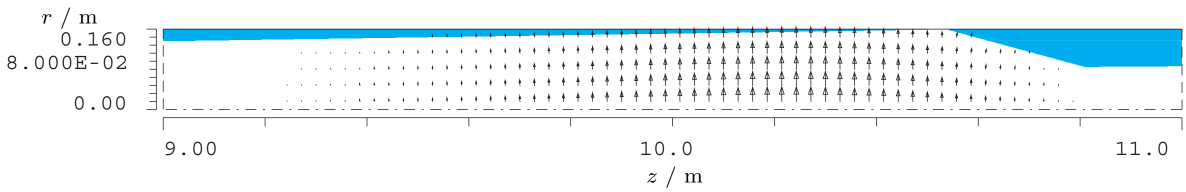

Figure 16: Electric field of dipole mode EE-1 in the CMS vacuum chamber.

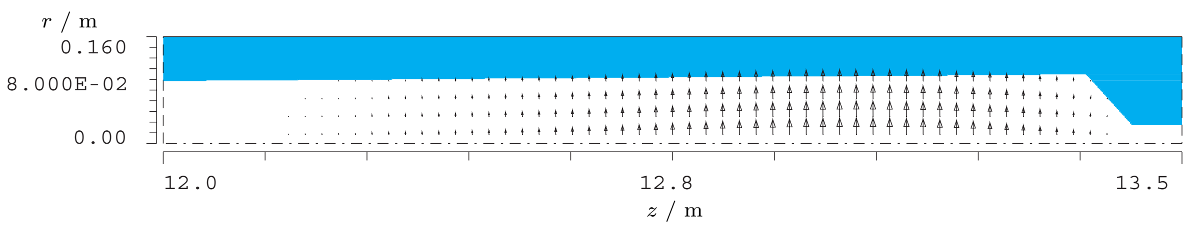

Figure 17: Electric field of dipole mode EE-16 in the CMS vacuum chamber.

for an radial offset of 1 cm. The loss parameters for an offset of 1 cm are at least a factor 100 smaller than the loss parameters of the monopole modes. The dipole modes with relatively large loss parameters are not trapped in a short region but extend over quite a long distance in the vacuum chamber. This is illustrated for the mode EE-36 (f = 1078.1 MHz) in Fig. 19. The electric field of the mode is shown in three regions of the CMS vacuum chamber. The MAFIA model of the CMS vacuum chamber is plotted together the longitudinal electric field (r=1 cm) of mode EE-36 in Fig. 20.

To verify the numerical accuracy of the results the estimate of the frequency of the highest searched eigenvalue and the number of searched eigenvalues have been varied. Fifty eigenvalues have been calculated using estimates of 1.4 GHz and 3.0 GHz and seventy-five eigenvalues have been calculated using estimates of 1.6 GHz and 2.0 GHz. All results are shown in Fig. 21. The results with the somewhat crude estimate of 3.0 GHz differ significantly from the other results for all modes with a frequency larger than 1.2 GHz. All other results agree quite well. The results presented in tables 9 and 10 are taken from the calculation with an estimate of 1.6 GHz (plots of the electric fields of the first 50 modes from the 75 calculated modes are shown in appendix B).

The sum of all dipole loss parameters weighted with the power spectrum of the bunch $h(\omega)$ (see Eqn. (2)) is

$$k^{(1)}_{||\mathrm{modes}} = \sum_n k^{(1)}_{||n}\, h(\omega_n) = 0.15\ \frac{\mathrm{V}}{\mathrm{pC\,m^2}}, \tag{44}$$

taking into account all modes listed in tables 9 and 10.

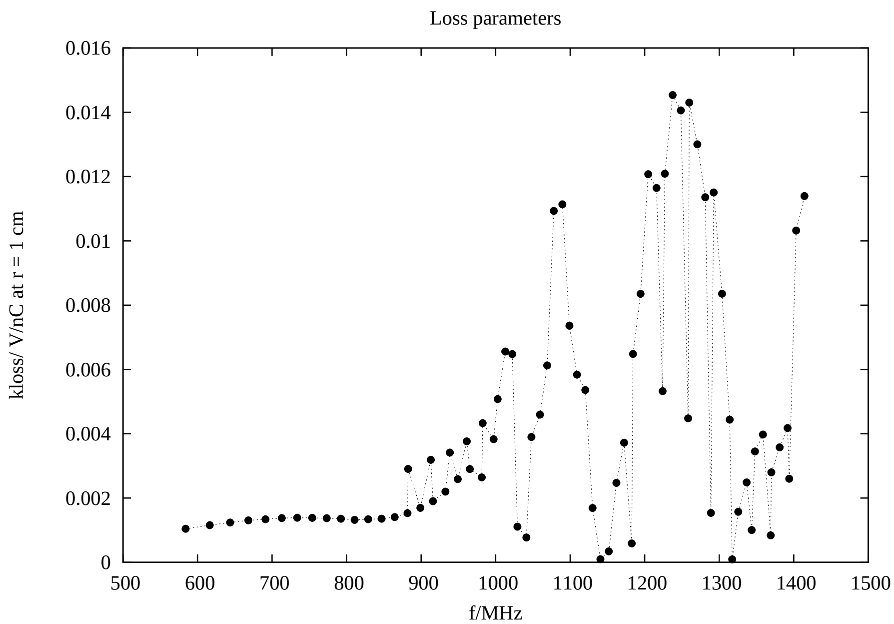

Figure 18: Plot of the loss parameters of the dipole modes at an offset of $r = 1$ cm versus frequency using the data from Tables 9 and 10. (The dotted line is intended only to guide the eye.)

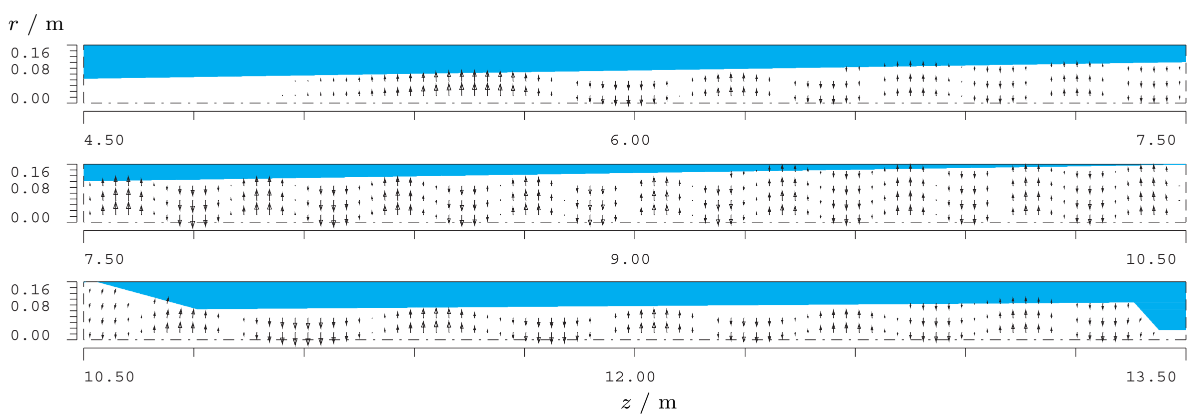

Figure 19: Electric field of dipole mode EE-36 in the CMS vacuum chamber.

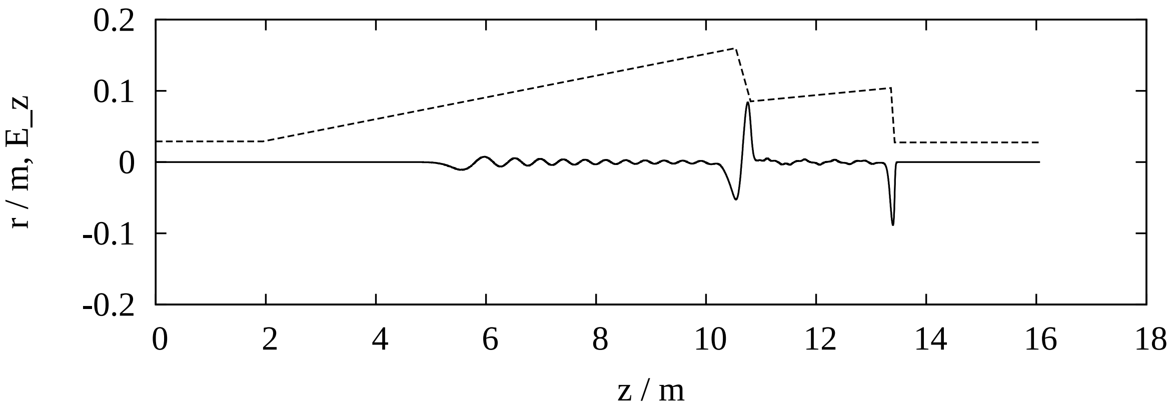

Figure 20: Longitudinal electric field (at $r = 1$ cm) of mode EE-36 in the CMS vacuum chamber.

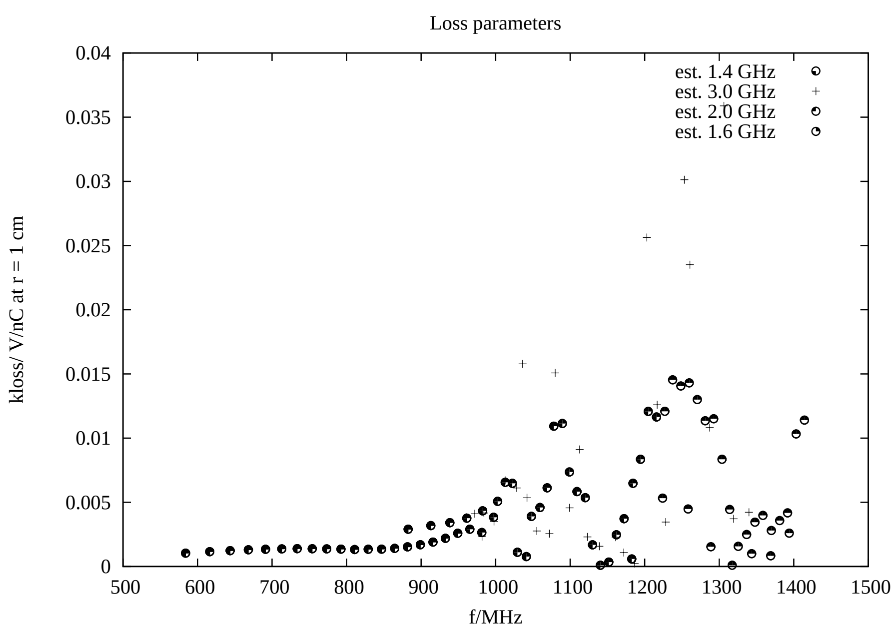

Figure 21: Plot of the loss parameters of the dipole modes at an offset of $r = 1$ cm versus frequency using the data from calculations with different estimates of the frequency of the highest searched eigenvalue.

Mode	f /MHz	$k^{(1)}(r)/r^2$ /(V/(nC m^2))	G_1 /Ohm	Q_{Cu}	Q_{Steel}	$Z_\perp$ /kOhm/m
EE- 1	584.0	10.4	261.827	41500	6640	3.08
EE- 2	616.4	11.6	273.406	42200	6750	3.12
EE- 3	643.7	12.4	282.985	42800	6840	3.11
EE- 4	668.3	13.1	291.565	43200	6920	3.07
EE- 5	691.3	13.4	299.441	43700	6980	2.98
EE- 6	713.0	13.8	306.779	44000	7050	2.90
EE- 7	733.8	13.9	313.774	44400	7100	2.78
EE- 8	753.9	13.8	320.394	44700	7160	2.65
EE- 9	773.4	13.7	326.786	45000	7210	2.51
EE-10	792.3	13.6	332.885	45300	7250	2.38
EE-11	810.9	13.2	338.800	45600	7300	2.23
EE-12	829.1	13.4	344.524	45900	7340	2.18
EE-13	846.9	13.6	350.174	46100	7380	2.12
EE-14	864.5	14.1	355.586	46400	7420	2.12
EE-15	881.8	15.3	361.025	46600	7460	2.23
EE-16	882.5	29.1	254.527	32800	5250	2.97
EE-17	899.0	16.9	366.052	46800	7490	2.38
EE-18	913.1	31.9	261.555	33200	5310	3.08
EE-19	915.9	19.0	371.277	47000	7520	2.59
EE-20	932.6	22.0	376.068	47200	7550	2.90
EE-21	938.5	34.2	267.345	33500	5350	3.15
EE-22	949.1	25.9	380.823	47400	7580	3.31
EE-23	961.3	37.7	272.569	33700	5390	3.34
EE-24	965.4	29.0	384.936	47500	7600	3.59
EE-25	981.4	26.4	377.092	46100	7380	3.07
EE-26	982.5	43.3	283.380	34700	5540	3.77
EE-27	997.2	38.3	384.257	46600	7460	4.37
EE-28	1002.6	50.8	287.502	34800	5570	4.27
EE-29	1012.8	65.6	384.861	46400	7420	7.20
EE-30	1022.3	64.8	307.264	36800	5890	5.55
EE-31	1029.2	11.1	383.042	45800	7320	1.17
EE-32	1041.3	7.7	352.255	41800	6690	0.73
EE-33	1048.0	39.0	362.253	42900	6860	3.70
EE-34	1059.4	46.0	387.941	45700	7310	4.55
EE-35	1069.0	61.2	365.983	42900	6860	5.58
EE-36	1078.1	109.3	395.230	46100	7380	10.54
EE-37	1089.5	111.4	395.899	46000	7360	10.49
EE-38	1098.9	73.6	392.352	45400	7260	6.72
EE-39	1109.1	58.4	411.714	47400	7580	5.46

Table 9: Dipole modes of the CMS vacuum chamber.

Mode	f /MHz	$k^{(1)}(r)/r^2$ /(V/(nC m^2))	G_1 /Ohm	Q_{Cu}	Q_{Steel}	$Z_\perp$ /kOhm/m
EE-40	1120.3	53.6	411.507	47100	7540	4.89
EE-41	1130.1	16.9	413.423	47100	7540	1.52
EE-42	1140.5	1.0	426.490	48400	7740	0.09
EE-43	1151.8	3.4	428.854	48400	7750	0.30
EE-44	1162.0	24.7	431.644	48500	7770	2.16
EE-45	1172.3	37.2	443.973	49700	7950	3.27
EE-46	1182.7	5.9	597.881	66600	10660	0.68
EE-47	1184.2	64.8	502.507	56000	8960	6.29
EE-48	1194.4	83.5	449.415	49800	7970	7.09
EE-49	1204.8	120.7	457.296	50500	8080	10.21
EE-50	1215.9	116.5	462.682	50900	8140	9.74
EE-51	1224.0	53.3	708.804	77700	12420	6.70
EE-52	1227.1	120.9	468.264	51200	8200	10.00
EE-53	1237.6	145.4	473.350	51600	8250	11.89
EE-54	1248.5	140.6	477.885	51800	8290	11.35
EE-55	1258.2	44.8	725.904	78400	12550	5.39
EE-56	1259.8	143.0	480.708	51900	8310	11.37
EE-57	1270.6	130.0	487.587	52400	8390	10.26
EE-58	1281.2	113.6	493.826	52900	8460	8.89
EE-59	1288.9	15.4	730.306	78000	12480	1.75
EE-60	1292.6	115.1	496.257	52900	8460	8.85
EE-61	1303.6	83.6	501.082	53200	8510	6.35
EE-62	1314.1	44.4	523.910	55400	8860	3.46
EE-63	1317.5	1.0	707.978	74800	11960	0.10
EE-64	1325.6	15.7	511.207	53800	8610	1.17
EE-65	1336.8	24.9	514.438	53900	8630	1.82
EE-66	1343.5	10.0	736.694	77000	12330	1.04
EE-67	1347.9	34.5	526.657	55000	8800	2.54
EE-68	1358.7	39.8	525.447	54600	8740	2.86
EE-69	1369.1	8.4	718.757	74500	11910	0.81
EE-70	1370.0	28.0	547.471	56700	9070	2.06
EE-71	1381.1	35.8	533.216	55000	8800	2.51
EE-72	1391.7	41.7	569.985	58600	9370	3.07
EE-73	1393.8	26.0	705.997	72500	11600	2.36
EE-74	1403.2	103.2	543.984	55700	8910	7.09
EE-75	1414.3	114.0	546.615	55700	8910	7.71

Table 10: Dipole modes of the CMS vacuum chamber.

3.3 Transient and Resonant Losses due to Monopole HOMs

The sum of all loss parameters weighted with the bunch spectrum $h(\omega)$ is

$$k_{||\mathrm{modes}} = \sum_n k_{||n}\, h(\omega_n) = 1.13\ \frac{\mathrm{V}}{\mathrm{nC}}, \tag{45}$$

taking into account all modes listed in tables 7 and 8. A plot of the quantity $k_{||n}\, h(\omega_n)$ versus the mode frequency is shown in Fig. 22. Using the sum of the loss parameters we can calculated the **transient power loss** to the modes as:

$$P_{loss} = N_b\, f_R\, {q_b}^2\, k_{||\mathrm{modes}} = 12\,\mathrm{W}, \tag{46}$$

where N_b is total number of bunches, f_R the revolution frequency and q_b the bunch charge (see Table 1). Here we have assumed that the losses from each bunch add up over one turn. Since we have calculated the modes in one half of the CMS vacuum chamber the total

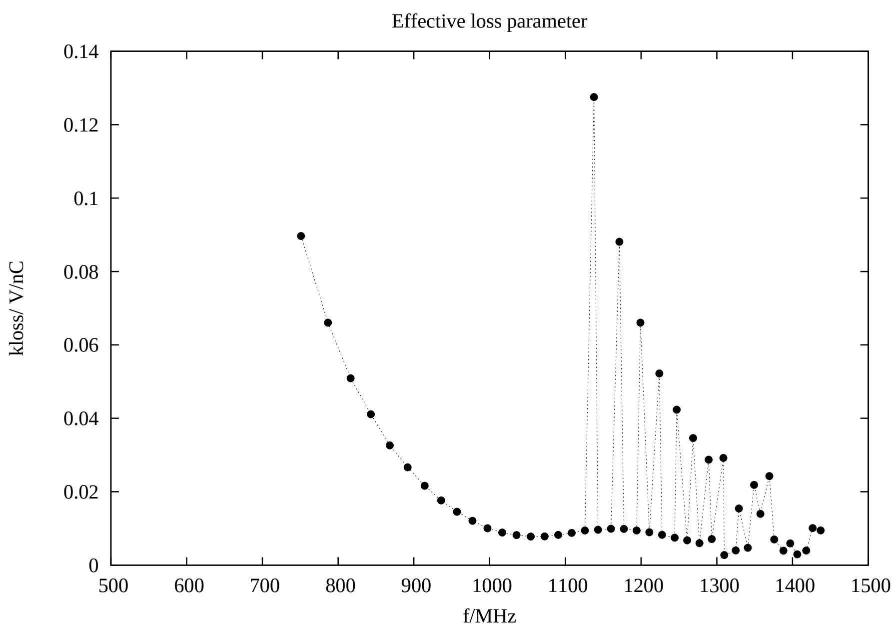

Figure 22: The loss parameter weighted with the bunch spectrum $h(\omega)$ plotted versus the mode frequency using the data from Tables 7 and 8. (The dotted line is intended only to guide the eye.)

transient power loss is twice the number calculated in Eqn. (46) or 24 W.

A mode may be resonantly excited when the mode frequency is close to a harmonic of the bunch repetition frequency

$$f_{rep} = \frac{1}{\Delta t} = \frac{h\,c}{C_R\,10} \approx 40\,\mathrm{MHz}, \tag{47}$$

where Δt is the bunch to bunch spacing, which is equal to 10 rf-buckets or about 25 ns. (C_R is the circumference, h the harmonic number and c the velocity of light, see Table 1). For each mode with frequency f we have calculated the quantity

$$f_{modulo} = mod(\frac{f}{f_{rep}}, 1). \tag{48}$$

The results are plotted versus the mode frequency, see Fig. 23. All frequencies of the MAFIA-model of the CMS vacuum chamber are not multiples of the bunch repetition frequency.

Furthermore the effective shunt impedance R_s and the width of the resonance $\Delta\omega$ are calculated using the conductivity of stainless steel to obtain the Q-value:

$$R_s = \frac{2\,k_{||}}{\omega}\,h(\omega)\,Q_{Steel}, \qquad \Delta\omega = \frac{\omega}{2\,Q_{Steel}}. \tag{49}$$

The results are shown in Fig. 24 and Fig. 25.

If a mode is resonantly excited the power loss in that mode will be

$$P_{res} = \frac{1}{2}\,R_s\,{I_{tot}}^2. \tag{50}$$

Using the effective shunt impedance R_s for steel and the total beam current of $I_{tot} = 0.582\,\mathrm{A}$ the resonant power is plotted for each mode in Fig. 26. In the worst case the beam can put a power of up-to 65 W into one mode. But from our MAFIA-model of the CMS vacuum chamber we do not have the indication that any mode is excited resonantly.

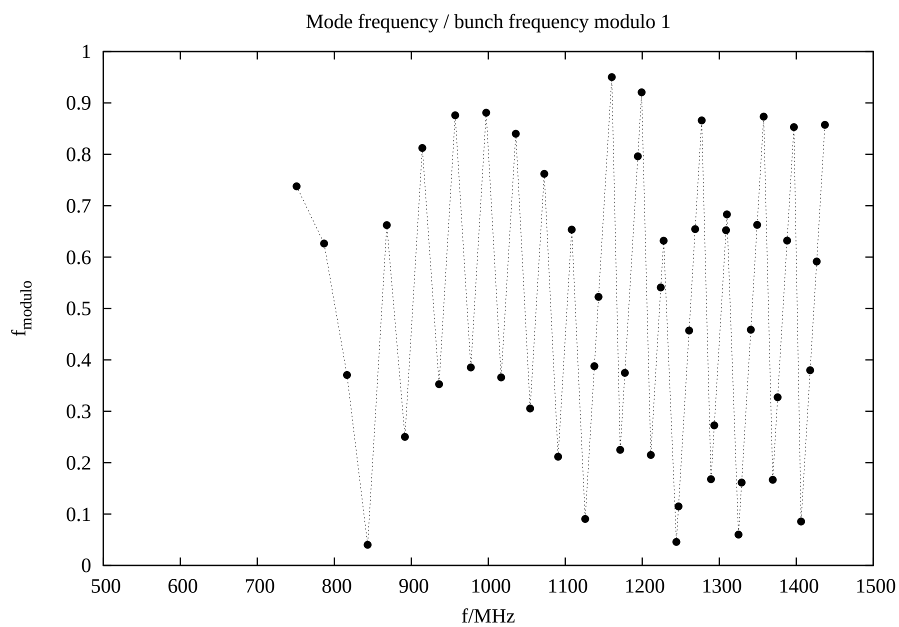

Figure 23: The mode frequency divided by the bunch repetition frequency modulo 1 is plotted versus the mode frequency using the data from Tables 7 and 8. (The dotted line is intended only to guide the eye.)

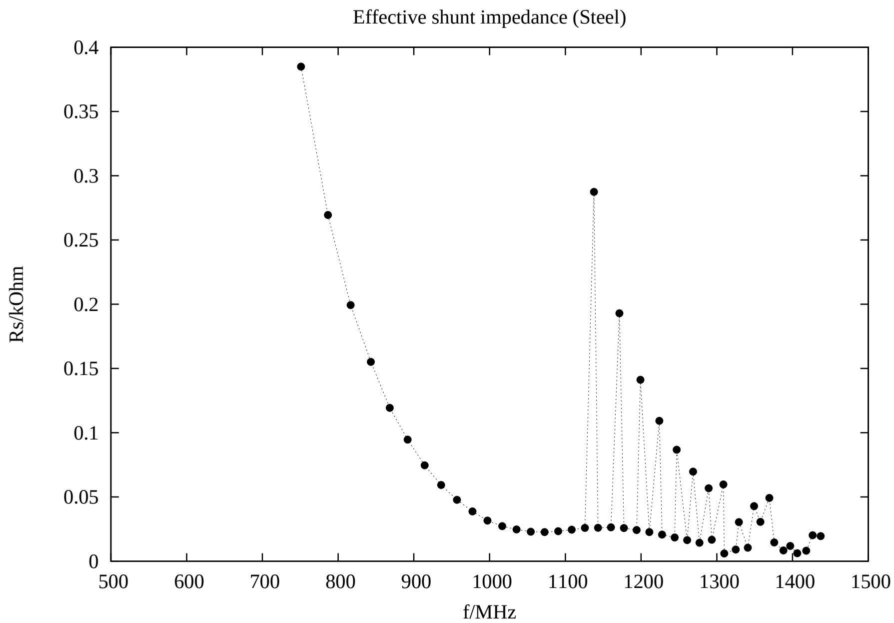

Figure 24: The effective shunt impedance $R_s\,h(\omega)$ plotted versus the mode frequency using the data from Tables 7 and 8. (The dotted line is intended only to guide the eye.)

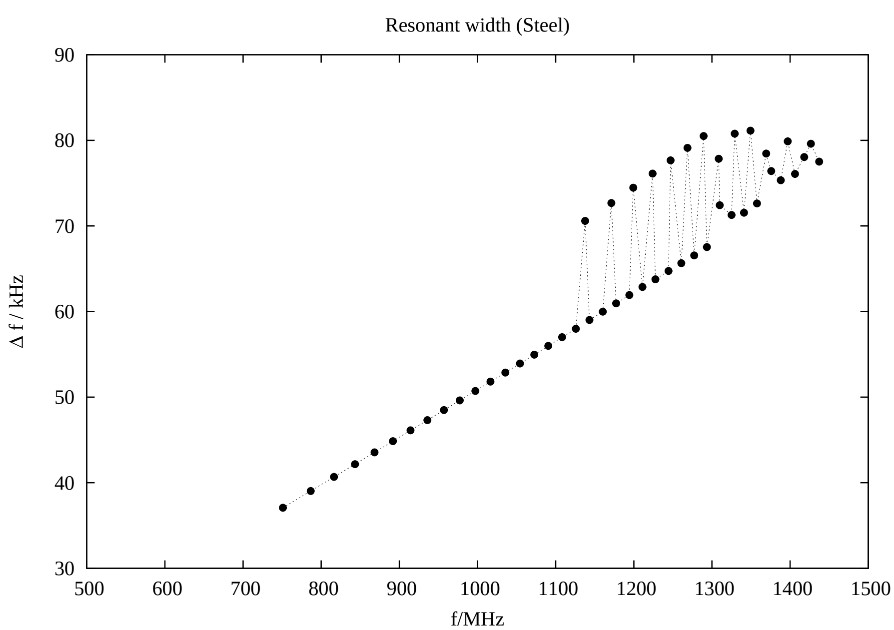

Figure 25: Resonant width $f/(2\,Q)$ versus the mode frequency using the data from Tables 7 and 8. (The dotted line is intended only to guide the eye.)

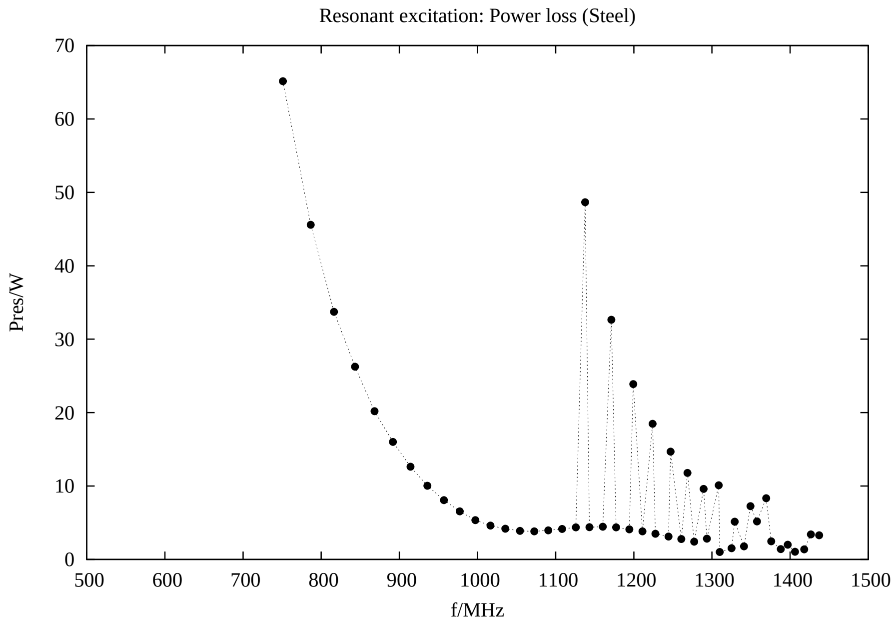

Figure 26: Resonant power loss versus the mode frequency using the data from Tables 7 and 8. (The dotted line is intended only to guide the eye.)

4 Wakefields

Since the CMS vacuum chamber is rotationally symmetric with respect to the longitudinal axis it is convenient to use a two dimensional (r, z) computer code for numerical wakefield calculations. The ECHO2D code [19, 20] was used to calculate the Monopole and Dipole wakefield of the CMS vacuum chamber. The geometry is shown in Fig. 27. A basic criteria

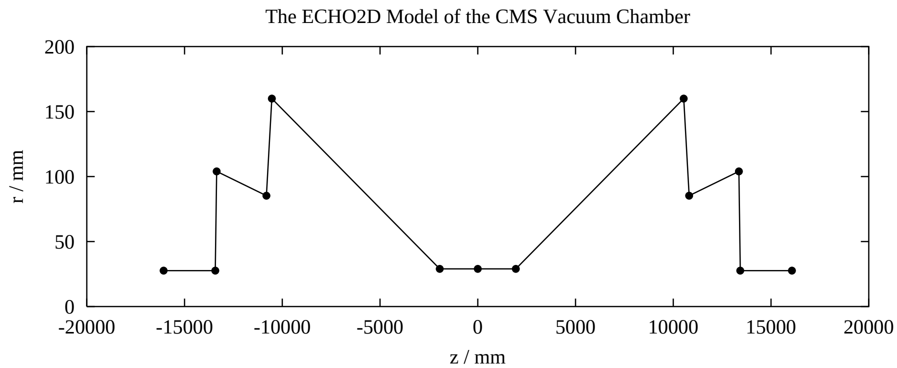

Figure 27: Schematic representation of the ECHO2D model of the CMS vacuum chamber. All dimensions are in mm. The interaction point (IP) is at $z = 0$ mm.

to ensure a small numerical error of wakefield calculations is [21]:

$$\frac{\Delta z^2 \, l}{{\sigma_z}^3} < 1, \tag{51}$$

where Δz is the step size, σ_z the rms bunch length and l is the total length of the vacuum chamber. For the CMS vacuum chamber the total length is about 32 m and the rms bunch length is 7.5 cm. For the wake field calculation a step size of $\Delta z = 2$ mm in the longitudinal and of $\Delta r = 1$ mm have been used which fulfill the criteria (51).

The longitudinal (monopole) wake potential for a bunch length of $\sigma_z = 7.5$ cm is shown in Fig. 28. The total loss parameter is

$$k^{(0)}_{||\mathrm{tot}} = \int ds \; W^{(0)}_{\|}(s) \; g(s) \; = 2.36 \; \frac{\mathrm{V}}{\mathrm{nC}}, \tag{52}$$

where $g(s)$ is the normalized charge density of the bunch, see Eqn.(1). The monopole and dipole modes have only been calculated for the right part of the CMS vacuum chamber (see Fig. 7). The total loss parameter from the time domain calculation has to be compared with twice the sum of all 50 monopole mode loss parameters weighted with the bunch spectrum, which is

$$2 \; k_{||\mathrm{modes}} = 2.26 \; \frac{\mathrm{V}}{\mathrm{nC}}. \tag{53}$$

The good agreement between the total loss parameter $k^{(0)}_{||\mathrm{tot}}$ and the weighted sum of the loss parameter $2 \; k_{||\mathrm{modes}}$ shows that the interaction of the bunch ($\sigma_z = 7.5$ cm) and the CMS vacuum chamber is dominated by the trapped monopole modes, which are listed in Tables 7 and 8.

The total loss parameter $k^{(0)}_{\|\mathrm{tot}}$ characterizes the resistive part of the impedance. The inductive part of the impedance can be calculated from the averaged gradient of the wake potential of a Gaussian bunch:

$$\begin{aligned} k^{(0)}(1)_{\|\mathrm{tot}} &= \int ds\ \frac{d}{ds} W^{(0)}_{\|}(s)\ g(s) \\ &= -\int ds\ W^{(0)}_{\|}(s)\ \frac{d}{ds} g(s) \\ &= 0.507\ \frac{\mathrm{V}}{\mathrm{pC\,m}}. \end{aligned} \tag{54}$$

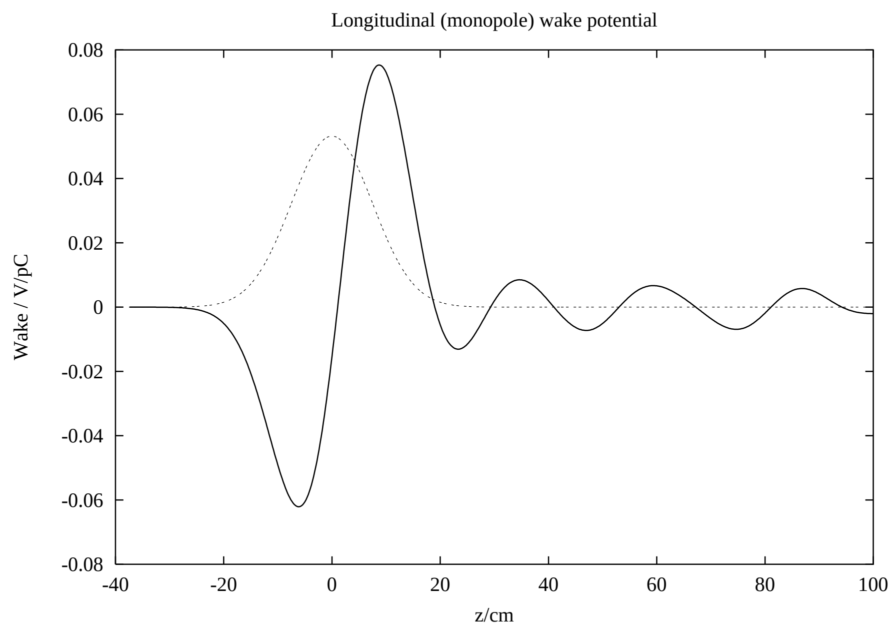

Figure 28: Longitudinal (monopole) wake potential of the CMS vacuum chamber. The wake has been calculated with the ECHO2D code for an rms bunch length of 7.5 cm. The bunch shape is also shown (in arbitrary units).

The longitudinal and transverse *dipole* wake potentials are shown in Fig. 29 and Fig. 30 respectively. The total dipole loss parameter is:

$$k^{(1)}_{\|\mathrm{tot}} = \int ds\ W^{(1)}_{\|}(s)\ g(s)\ = 0.412\ \frac{\mathrm{V}}{\mathrm{pC\ m}^2}, \tag{55}$$

which is about 30 % larger than twice the weighted sum of the loss parameters of the 50 dipole modes from Eqn. (44). The 50 modes, listed in Tables 9 and 10, contribute about 75 % to the interaction of the bunch with dipole fields in the CMS vacuum chamber.

The total (dipole) kick parameter is

$$k^{(1)}_{\perp} = \int ds\ W^{(1)}_{\perp}(s)\ g(s)\ = 2.36\ \frac{\mathrm{V}}{\mathrm{pC\ m}}. \tag{56}$$

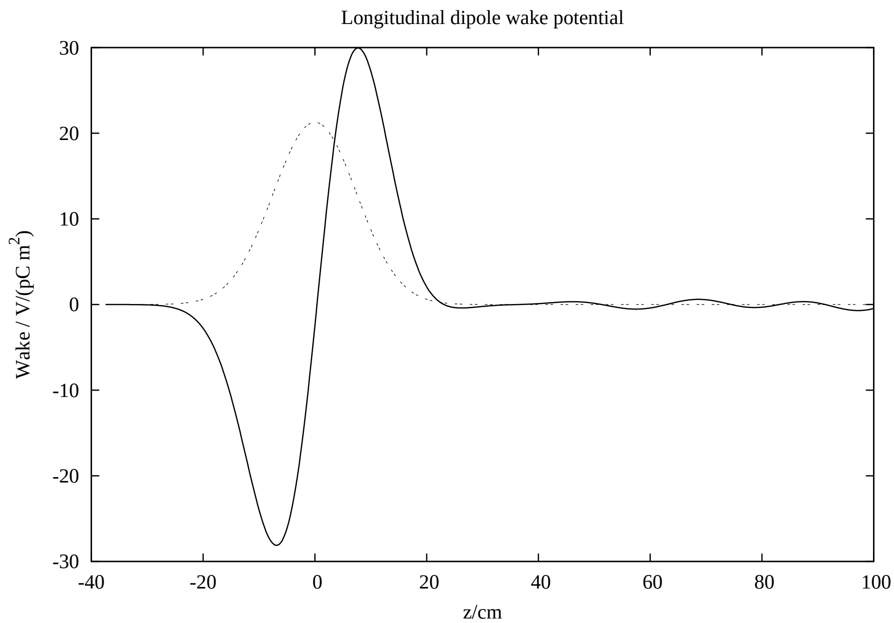

Figure 29: Longitudinal dipole wake potential of the CMS vacuum chamber. The wake has been calculated with the ECHO2D code for an rms bunch length of 7.5 cm. The bunch shape is also shown (in arbitrary units).

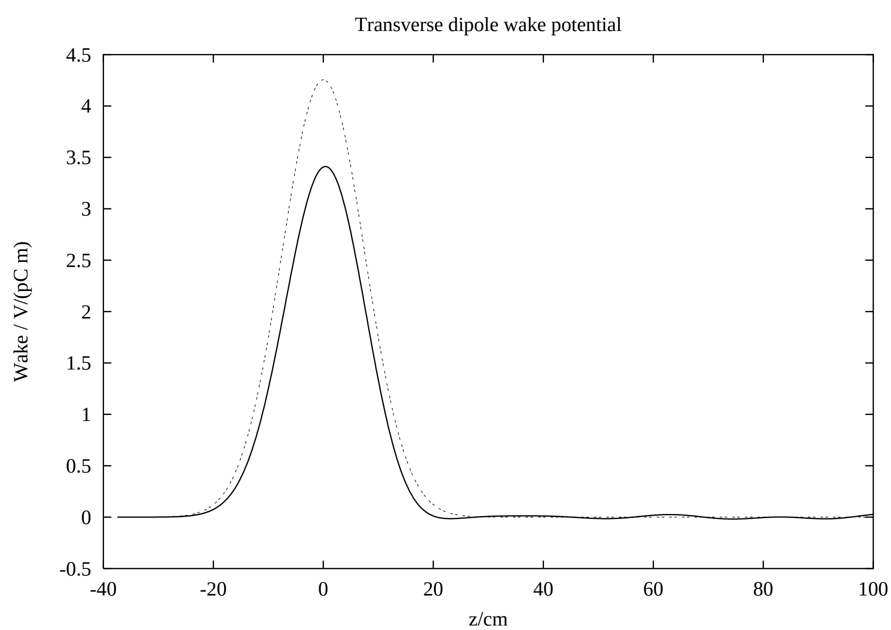

Figure 30: Transverse dipole wake potential of the CMS vacuum chamber. The wake has been calculated with the ECHO2D code for an rms bunch length of 7.5 cm. The bunch shape is also shown (in arbitrary units).

The parameters $k_\perp^{(1)}$ and $k^{(0)}(1)_{\|\mathrm{tot}}$ are closely related to the transverse and longitudinal *effective* impedance of the CMS vacuum chamber. The transverse impedance is (see [22])

$$(Z_\perp)_{\mathrm{eff}} = 2\sqrt{\pi}\,\frac{\sigma_z}{c}\,k_\perp^{(1)} = 2.1\,\frac{\mathrm{kOhm}}{\mathrm{m}}. \tag{57}$$

The effective longitudinal impedance is approximately

$$\Big(-\Im[Z_\|]/n\Big)_{\mathrm{eff}} \approx \omega_0\,4\sqrt{\pi}\,\frac{{\sigma_z}^2}{c^2}\,k^{(0)}(1)_{\|\mathrm{tot}} \ = 1.19\cdot 10^{-3}\,\mathrm{Ohm}, \tag{58}$$

where $\omega_0 = 2\,\pi\,11.245\,\mathrm{kHz}$ is the revolution frequency of the LHC and $n = \omega/\omega_0$.

The equation (58) is based on the assumption that the longitudinal (monopole) impedance can be approximated for small frequencies ω as:

$$Z_\|(\omega) \approx -i\,\omega\,L, \tag{59}$$

with an inductance L. The corresponding wake potential for a Gaussian bunch is [23]

$$W_\|(s) = -L\,c^2\,\frac{d}{ds}g(s) \tag{60}$$

and the parameter $k(1)_\|$ is:

$$k(1)_\| = L\,\frac{1}{4\sqrt{\pi}}\,\frac{c^2}{{\sigma_z}^2}. \tag{61}$$

The effective impedance of the purely inductive impedance is:

$$\Big(Z_\|/n\Big)_{\mathrm{eff}} = \frac{\int d\omega\,(-i\,\omega_0\,L)\,h(\omega)}{\int d\omega\,h(\omega)} = -i\,\omega_0\,L. \tag{62}$$

Combining the results (62) and (61) gives the approximation (58) for the effective longitudinal impedance of CMS vacuum chamber.

5 Summary

The trapped Higher Order Modes and the Wake potentials of a Gaussian bunch in the vacuum chamber of the CMS experiment at the LHC have been calculated using a geometrical model which closely reflects the presently (in 2008) installed vacuum chamber. The basic rf-parameters of the monopole and dipole higher order modes (HOMs) are provide in Tables 7, 8, 9 and 10. Extensive graphical representations of the longitudinal electrical fields are given in appendices A and B.

The transient power loss to the modes is about 24 W while a resonant excitation of a mode can exceed this value. In the worst case the beam can put a power of up-to 65 W into one mode (see Fig. 26).

The longitudinal and transverse effective impedances of the CMS vacuum chamber have been estimated from loss and kick parameters which have been obtained from wakefield calculations: $(Z_\perp)_{\text{eff}} = 2.1\,\text{kOhm/m}$ and $\left(-\Im[Z_\parallel]/n\right)_{\text{eff}} = 1.19 \cdot 10^{-3}\,\text{Ohm}$.

It is interesting to compare the results from this report with the previously obtained results in [3] and [4], which reflects the difference in the geometry of the considered versions of the CMS vacuum chamber (see Fig. 5). A comparison of the loss parameters of the longitudinal modes is shown in Fig. 31. The data from Tables 5,6,7 and 8 of Ref. [3] correspond

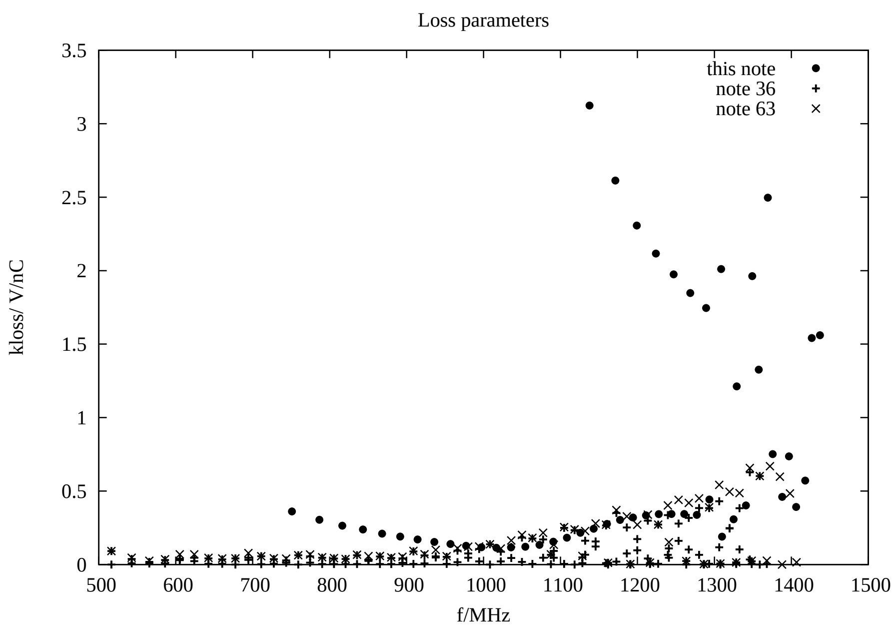

Figure 31: Plot of the loss parameters of the monopole modes versus frequency using the data from: Tables 7 and 8 (dark dots, this note); Tables 5,6,7 and 8 of Ref. [3] (crosses, note 36); Tables 3 and 4 of Ref. [4] (crosses, note 63).

to the vacuum chamber geometry from 1995 with a 2 m taper (see Fig. 5) and the data from Tables 3 and 4 of Ref. [4] correspond to the same geometry but are the sum of the two symmetry modes (E) and (H) of Ref. [3] (see page 5 of Ref. [4]). Using the frequency f, the shunt impedance R_s and the Q-value from the above mentioned Tables of Ref. [3, 4] the loss parameters of the modes have been calculated for each mode according to the formula:

$$k_{\|} = \frac{R_s \, 2\,\pi\, f}{2\, Q}. \tag{63}$$

These loss parameters are plotted together with the losses from Tables 7 and 8 of this report (see also Fig. 12). Significant differences between the loss parameters in this report and those previously reported can be found for several modes with relatively large loss parameters in the frequency range between 1100 MHz and 1450 MHz. These modes have been identified as trapped modes in the HF-pipe region of the CMS vacuum chamber (see Fig. 13 and Appendix A).

A comparison of the results for the total loss parameter and the incoherent losses is given in Table 11. The total loss parameter has been calculated from the longitudinal wake potential (see Eqn. 52 for the geometry shown in Fig. 27). The corresponding value for the CMS chamber geometry from 1995 has been taken from Table 1 of Ref. [4]. The transient (incoherent) power loss has been calculated for the beam parameters from Table 1 which differ slightly from the parameters of Ref. [4]. The value for the incoherent power loss for the total loss parameter of Ref. [4] has been calculated for the parameters from Table 1. The original value of 8.98 W from Ref. [4] has been added in brackets.

Parameter	Unit	this report	Ref. [4]	
$k^{(0)}_{\|\|\mathrm{tot}}$	V/nC	2.36	1.1	
$P_{incoh.}$	W	25.3	11.8	(8.98)

Table 11: Total loss parameter of the CMS vacuum chamber for the recent (2008) chamber geometry and the previously considered geometry for a rms bunch length of 7.5 cm.

An upper bound between 3.11 kW and 5.26 kW for the coherent losses has been given in Ref. [4] (page 6). For these bounds the Q-values for copper have been used, which are about a factor 6.25 larger than Q-values for stainless steel vacuum chambers. For stainless steel the upper bounds would be 498 W and 842 W for the modes in Ref. [4]. A corresponding quantity in this report is the resonant power loss which is shown in Fig. 26. The sum over all resonant power losses from Fig. 26 is:

$$\sum_{n=1}^{50} P_{res,n} = 529 \text{ W}, \tag{64}$$

which may be compared to the upper bound for the coherent losses from Ref. [4]. The calculations do not indicate that this worst case scenario is likely to occur during beam operation at the LHC since the modes are not resonantly excited (see also Fig. 23).

A comparison of the results from this report (Tab. 9 and 10) with the previously obtained results in [3] for the transverse impedance of the dipole modes is shown in Fig. 32. The (narrow band) transverse impedance of the dipole modes has been calculated for 75 modes according to Eqn. (43) for the presently used geometry of the CMS Vacuum chamber. The transverse impedance of 66 dipole modes calculated for a previously considered version of the CMS vacuum chamber are taken from Tables 15 and 16 of Ref. [3]. The modes with a larger transverse impedance (about 10 kOhm/m) are shifted to higher frequencies (1 GHz

$\cdots$ 1.3 GHz) compared to the previously obtained result [3]. The implication of the present results on the beam dynamics of the LHC will be discussed in a forthcoming report [24].

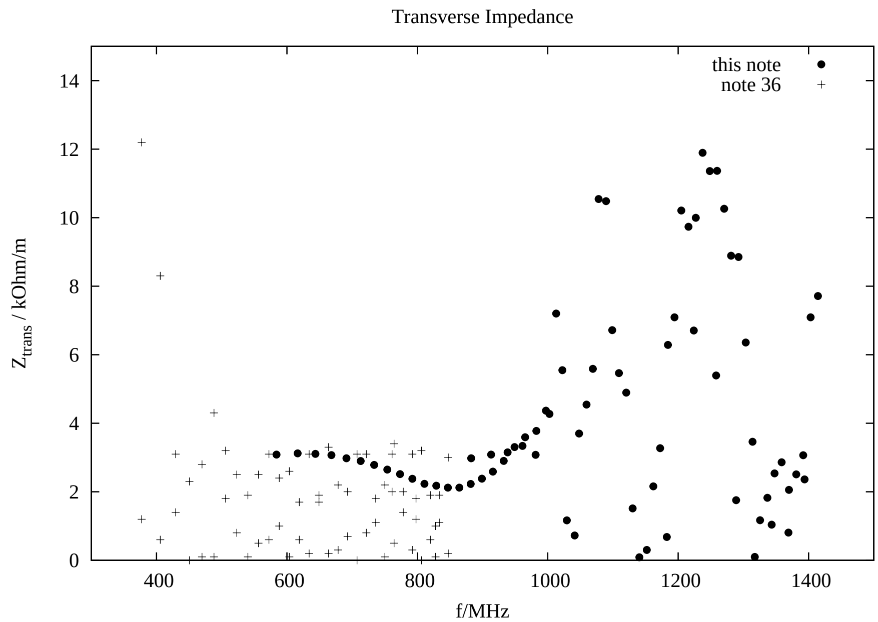

Figure 32: Plot of the transverse impedance of the dipole modes versus frequency using the data from: Tables 9 and 10 (dark dots, this note); Tables 15 and 16 of Ref. [3] (crosses, note 36).

Acknowledgment

I would like to thank Oliver Brüning for the invitation to work on "LHC Commissioning" in the Accelerator Beam Physics Group (ABP) and Elias Metral for his assistance as my supervisor during my stay from Aug. 6 to Sep. 6, 2008 at CERN. My thanks go to all colleagues of the ABP and other groups for their kind hospitality and support during my visit. My special thanks go to Werner Herr for his generous hospitality which made lodging in Geneva easy for me. Furthermore I would like to thank Wolfram Zeuner who provided all the details about the CMS vacuum chamber and Mark Lomperski for carefully reading the manuscript.

References

[1] O. Brüning (ed.), P. Collier (ed.), P. Lebrun (ed.), S. Myers (ed.), R. Ostojic (ed.), J. Poole (ed.), P. Proudlock (ed.), *LHC Design Report - Vol 1 the LHC Main Ring*, CERN-2004-003-V-1, 2004.

[2] O. Brüning, *Loss Factor and Longitudinal Higher Order Modes in the CMS Experimental Chamber*, CERN, LHC Project Note 14, October 1995.

[3] O. Brüning, *Longitudinal and transverse Modes in the CMS Experimental Chamber*, CERN, LHC Project Note 36, March 1996.

[4] O. Brüning, *Coherent Losses in the CMS Experimental Chamber*, CERN, LHC Project Note 63, March 1996.

[5] D. Angal-Kalinin, *Review of Coupled Bunch Instabilities in the LHC*, CERN, LHC Project Note 595, July 2002.

[6] M. Furman, H. Lee and B. Zotter, *Energy Loss Of Bunched Beams In SSC Rf Cavities*, Proceedings of 12th IEEE Particle Accelerator Conference (PAC), Washington, 16-19 Mar 1987, pp 1049.

[7] W. Zeuner, *CMS vacuum system*, private communication (2008).

[8] C. Benvenuti, *Non-evaporable Getters: From Pumping Strips to Thin Film Coatings*, Proceedings of 6th European Particle Accelerator Conference (EPAC), Stockholm, 22-26 June 1998.

[9] T. Weiland, R. Wanzenberg, *Wakefields and Impedances*, in: Joint US-CERN part. acc. school, Hilton Head Island, SC, USA, 7 - 14 Nov 1990 / Ed. by M Dienes, M Month and S Turner. - Springer, Berlin, 1992- (Lecture notes in physics ; 400) - pp.39-79.

[10] T. Weiland, *On the numerical solution of Maxwell's Equations and Applications in the Field of Accelerator Physics*, Part. Acc. 15 (1984), 245-292.

[11] *MAFIA Release 4 (V4.200)* CST AG, Bad Nauheimer Str. 19, 64289 Darmstadt, Germany.

[12] T. Weiland, *On the computation of resonant modes in cylindrically symmetric cavities*, NIM 216 (1983) 329-348.

[13] T. Weiland, *Comment on wake field computation in time domain*, DESY M-83-02, Feb. 1983.

[14] W.K.H. Panofsky, M. Phillips, *Classical Electricity and Magnetism*, Addison-Wesley, Reading Massachusetts 1962.

[15] P.B. Wilson *High Energy Electron Linacs: Application to Storage Ring RF Systems and Linear Colliders*, AIP Conference Proceedings 87, American Institute of Physics, New York (1982),p. 450-563.

[16] W.K.H. Panofsky, W.A. Wenzel, *Some consideration concerning the transverse deflection of charged particles in radio-frequency fields* , Rev. Sci. Inst. Vol 27, 11 (1956), 967.

[17] S. Calatroni, private communication (2004), CERN.

[18] D.R. Lide, Ed. *Handbook of Chemistry and Physics* , 79th edition, 1998-1999, CRC Press, Washington, D.C.

[19] I. Zagorodnov and T. Weiland, *TE/TM field solver for particle beam simulations without numerical Cherenkov radiation*, Phys. Rev. ST Accel. Beams **8** (2005) 042001.

[20] I. Zagorodnov, *Indirect methods for wake potential integration*, Phys. Rev. ST Accel. Beams **9** (2006) 102002 [arXiv:physics/0606049].

[21] M. Dohlus, private communication (2008).

[22] T. F. Günzel, *Transverse Coupling Impedance Of The Storage Ring At The European Synchrotron Radiation Facility*, Phys. Rev. ST Accel. Beams **9** (2006) 114402.

[23] A. Novokhatski and T. Weiland, *Inductive impedance and longitudinal instability*, Proceedings of the 7th European Particle Accelerator Conference (EPAC 2000), Vienna, Austria, 26-30 Jun 2000.

[24] E. Metral and R. Wanzenberg, *Wake and Higher Order Mode Computation for CMS Experimental Chamber at the LHC*, submitted to Particle Accelerator Conference, Vancouver 2009

A Electric fields of monopole modes

All electric fields are shown in arbitray units.

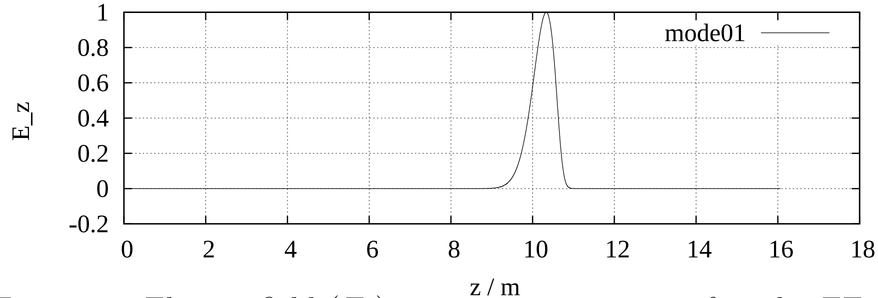

Figure 33: Electric field (E_z) at $r = 0$ cm versus z of mode: EE-01

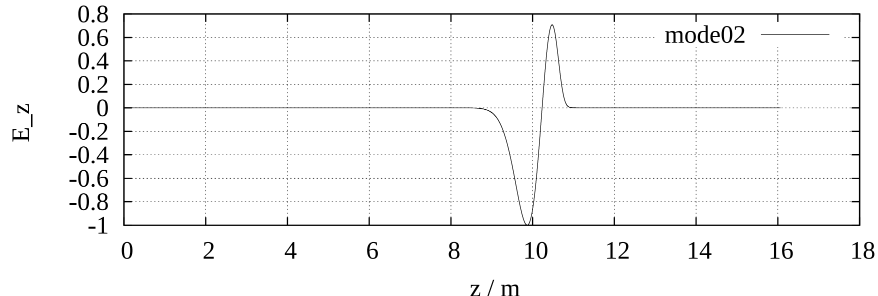

Figure 34: Electric field (E_z) at $r = 0$ cm versus z of mode: EE-02

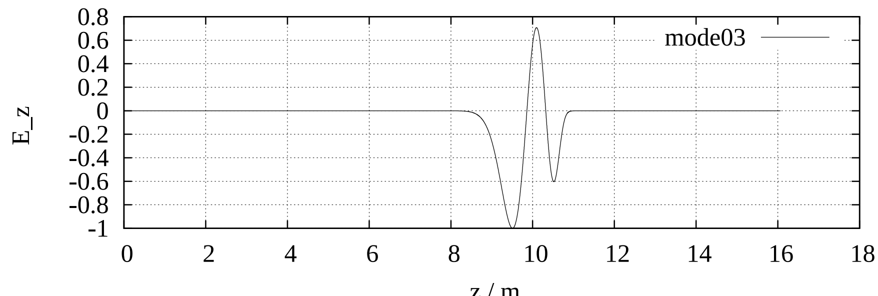

Figure 35: Electric field (E_z) at $r = 0$ cm versus z of mode: EE-03

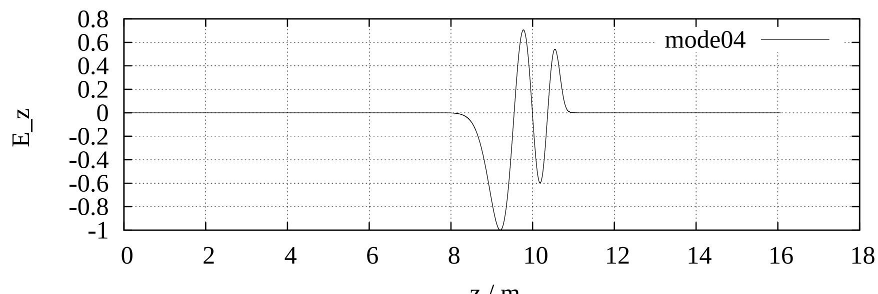

Figure 36: Electric field (E_z) at $r = 0$ cm versus z of mode: EE-04

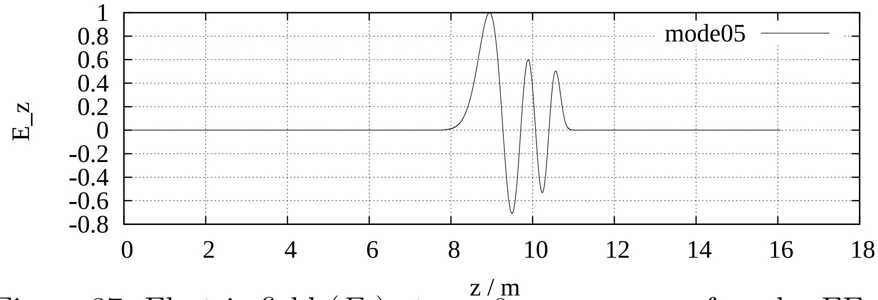

Figure 37: Electric field (E_z) at $r = 0$ cm versus z of mode: EE-05

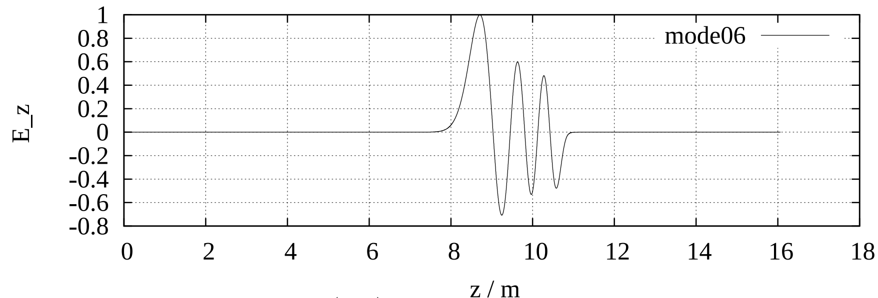

Figure 38: Electric field (E_z) at $r = 0$ cm versus z of mode: EE-06

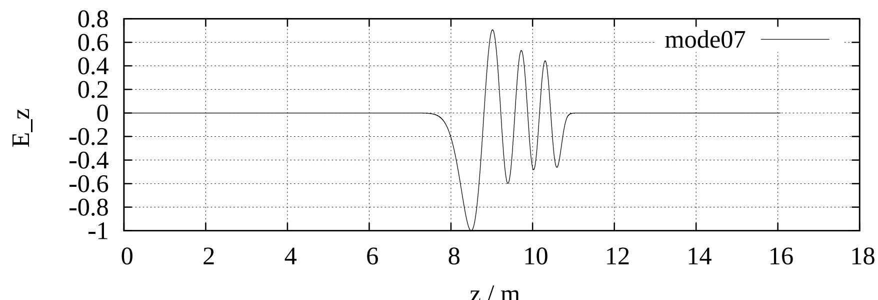

Figure 39: Electric field (E_z) at $r = 0$ cm versus z of mode: EE-07

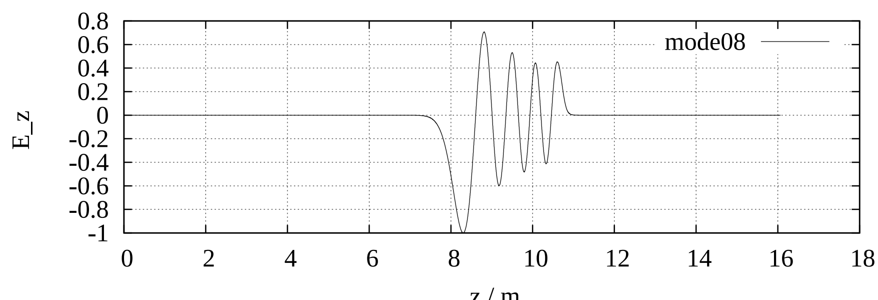

Figure 40: Electric field (E_z) at $r = 0$ cm versus z of mode: EE-08

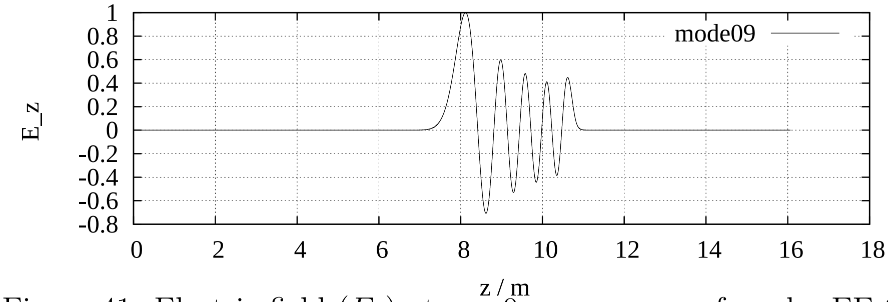

Figure 41: Electric field (E_z) at $r = 0$ cm versus z of mode: EE-09

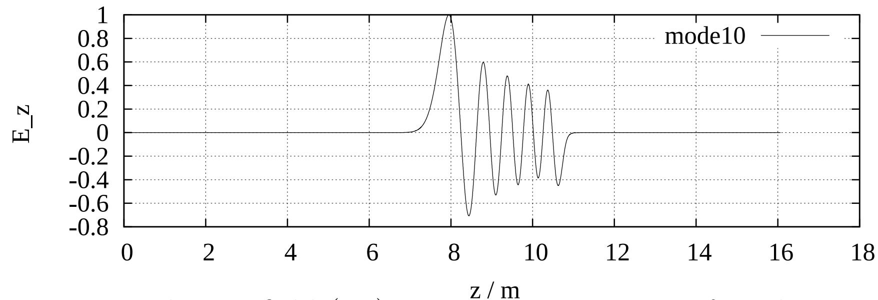

Figure 42: Electric field (E_z) at $r = 0$ cm versus z of mode: EE-10

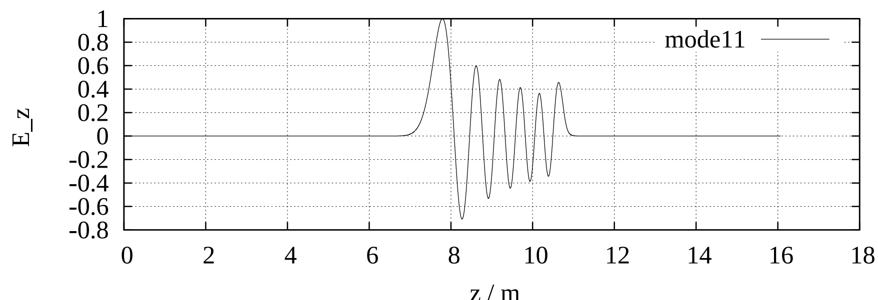

Figure 43: Electric field (E_z) at $r = 0$ cm versus z of mode: EE-11

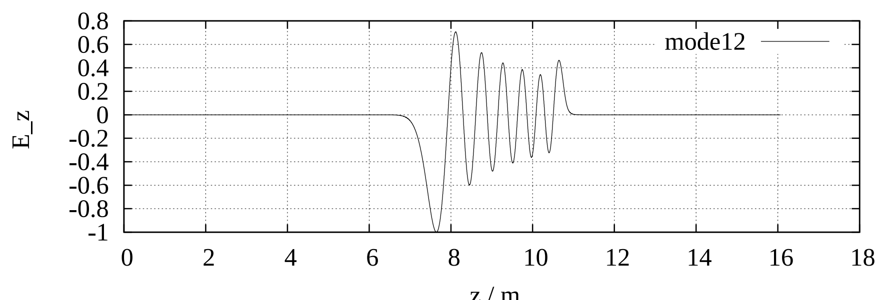

Figure 44: Electric field (E_z) at $r = 0$ cm versus z of mode: EE-12

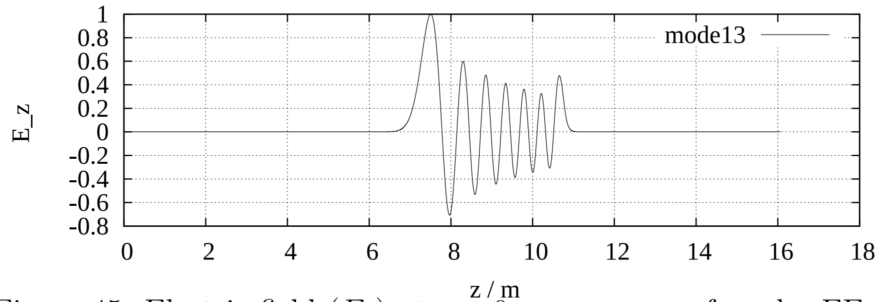

Figure 45: Electric field (E_z) at $r = 0$ cm versus z of mode: EE-13

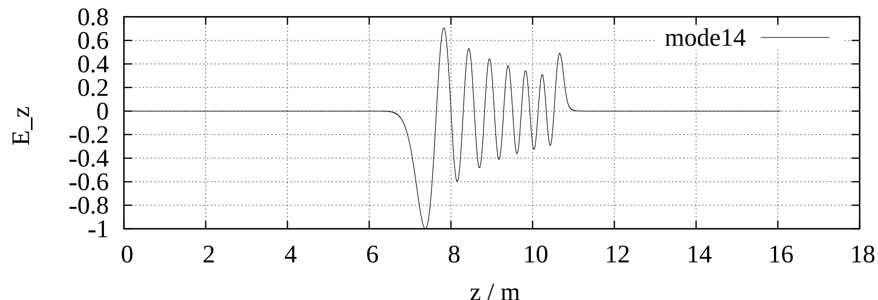

Figure 46: Electric field (E_z) at $r = 0$ cm versus z of mode: EE-14

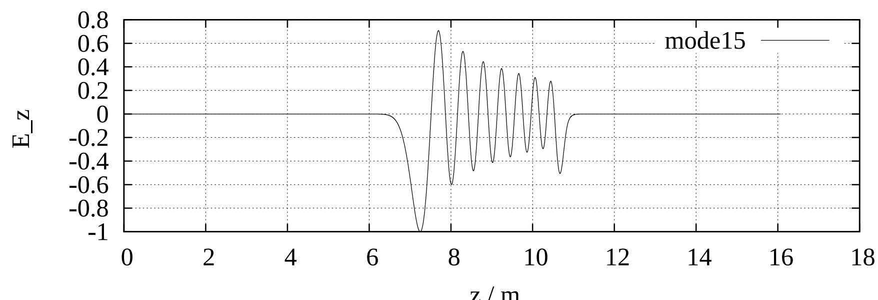

Figure 47: Electric field (E_z) at $r = 0$ cm versus z of mode: EE-15

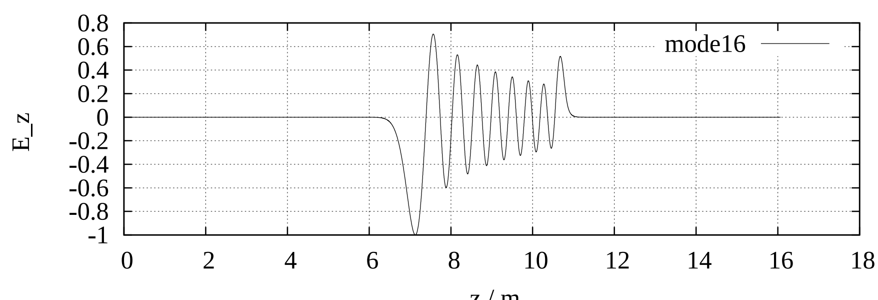

Figure 48: Electric field (E_z) at $r = 0$ cm versus z of mode: EE-16

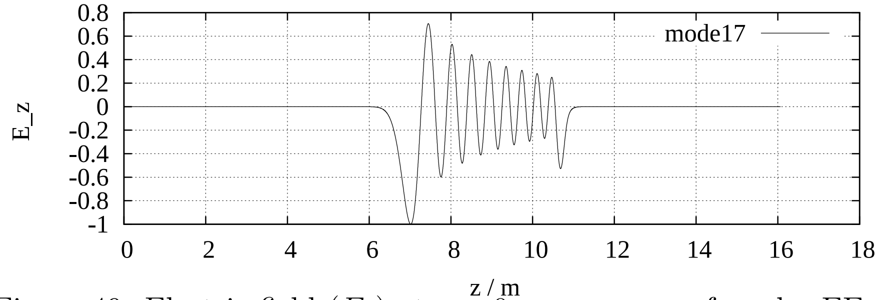

Figure 49: Electric field (E_z) at $r = 0$ cm versus z of mode: EE-17

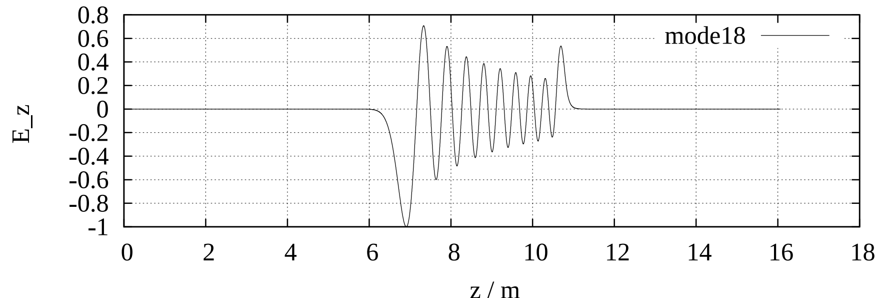

Figure 50: Electric field (E_z) at $r = 0$ cm versus z of mode: EE-18

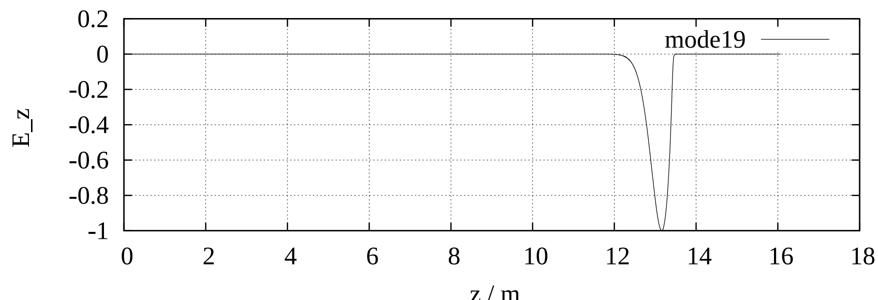

Figure 51: Electric field (E_z) at $r = 0$ cm versus z of mode: EE-19

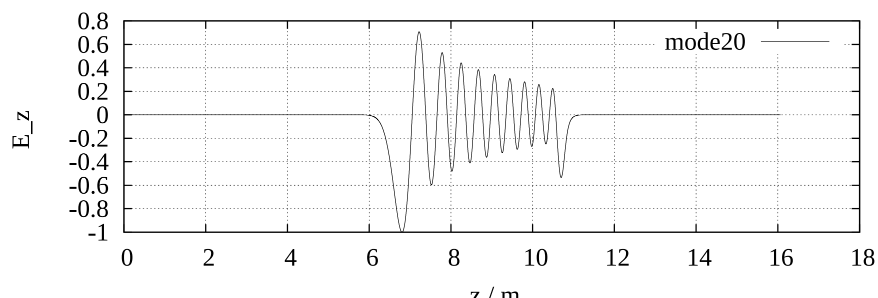

Figure 52: Electric field (E_z) at $r = 0$ cm versus z of mode: EE-20

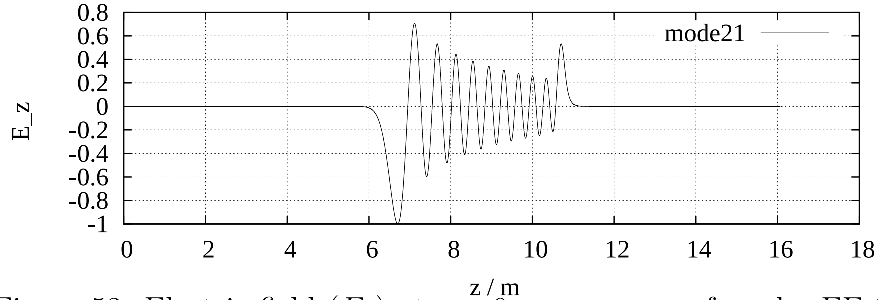

Figure 53: Electric field (E_z) at $r = 0$ cm versus z of mode: EE-21

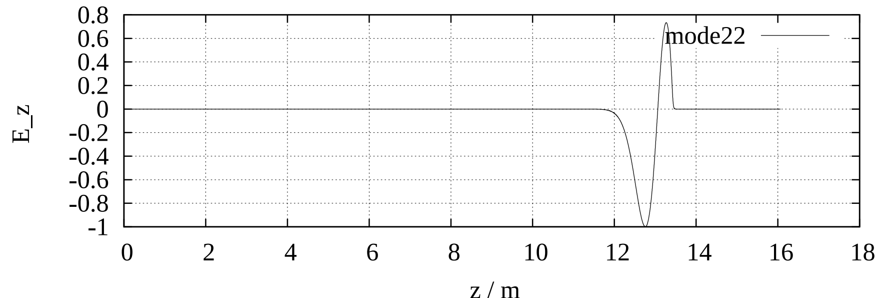

Figure 54: Electric field (E_z) at $r = 0$ cm versus z of mode: EE-22

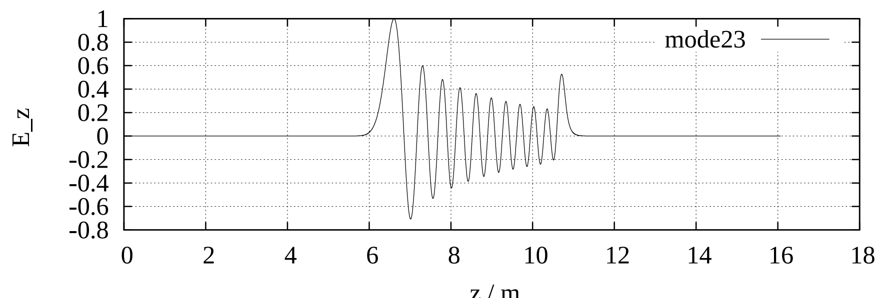

Figure 55: Electric field (E_z) at $r = 0$ cm versus z of mode: EE-23

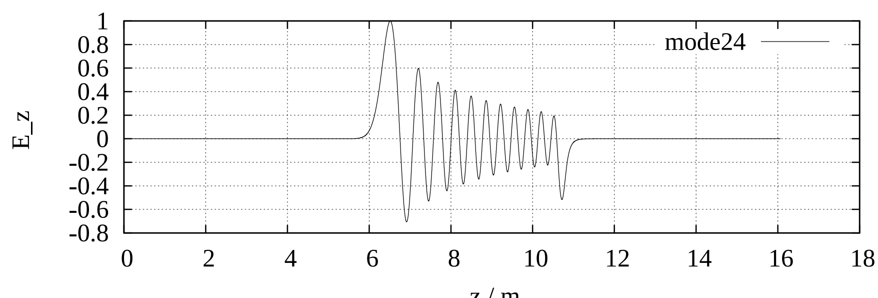

Figure 56: Electric field (E_z) at $r = 0$ cm versus z of mode: EE-24

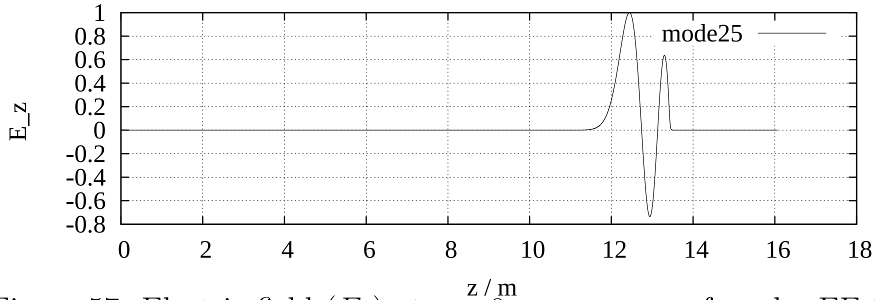

Figure 57: Electric field (E_z) at $r = 0$ cm versus z of mode: EE-25

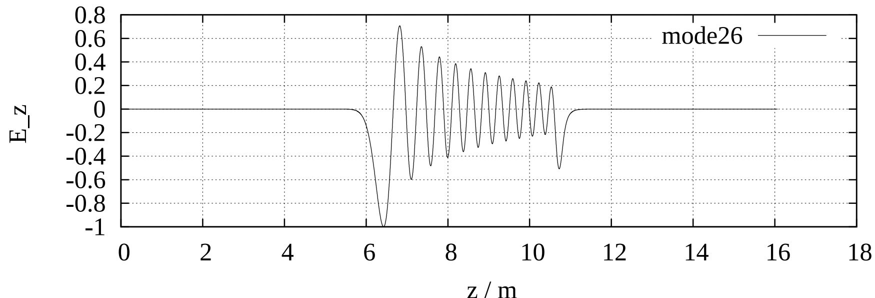

Figure 58: Electric field (E_z) at $r = 0$ cm versus z of mode: EE-26

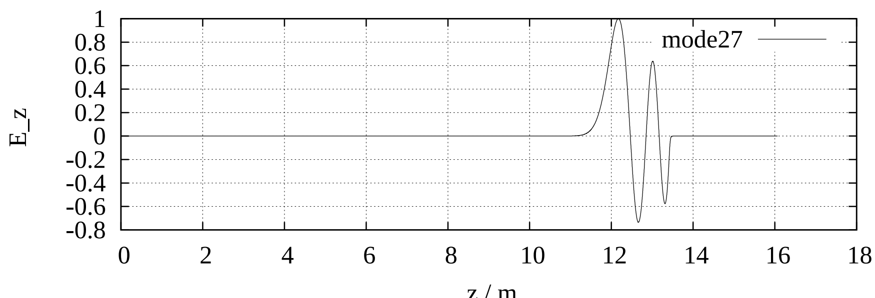

Figure 59: Electric field (E_z) at $r = 0$ cm versus z of mode: EE-27

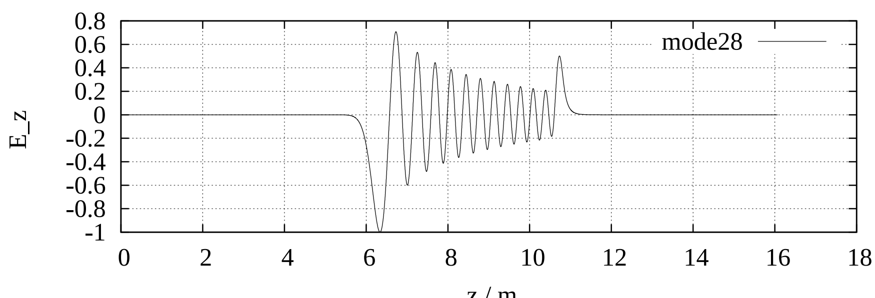

Figure 60: Electric field (E_z) at $r = 0$ cm versus z of mode: EE-28

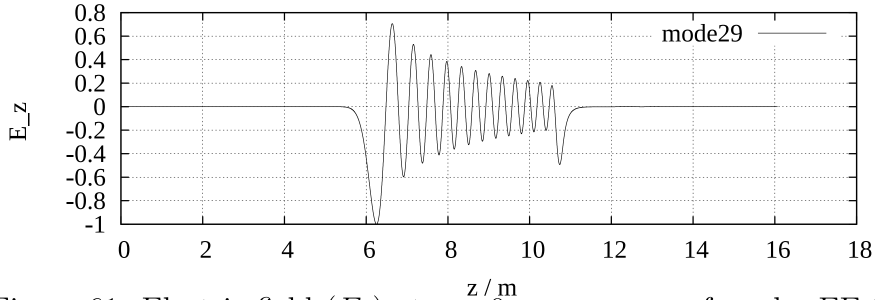

Figure 61: Electric field (E_z) at $r = 0$ cm versus z of mode: EE-29

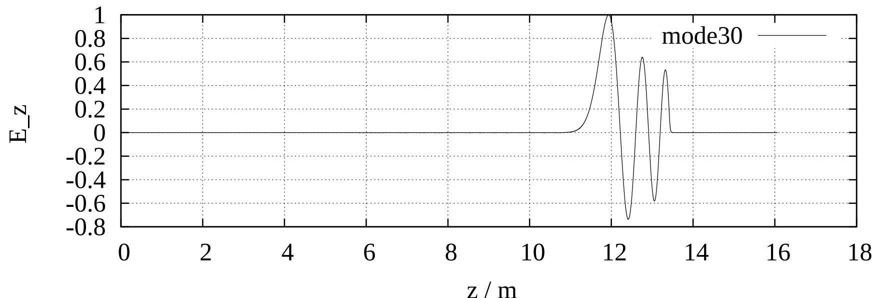

Figure 62: Electric field (E_z) at $r = 0$ cm versus z of mode: EE-30

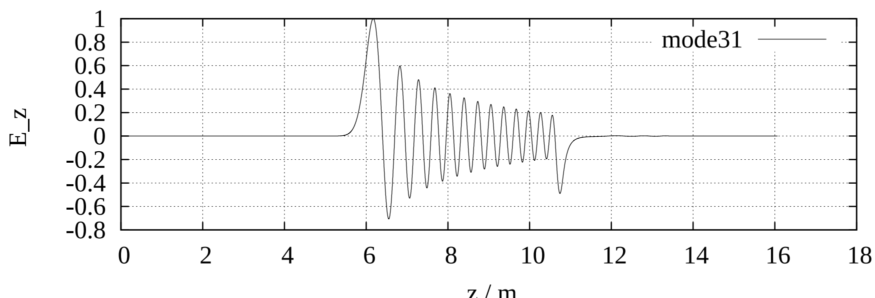

Figure 63: Electric field (E_z) at $r = 0$ cm versus z of mode: EE-31

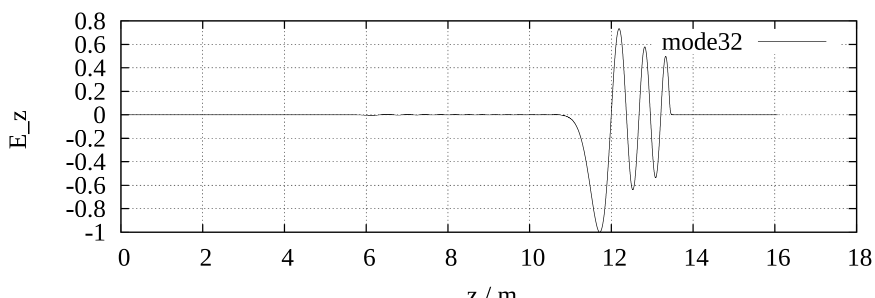

Figure 64: Electric field (E_z) at $r = 0$ cm versus z of mode: EE-32

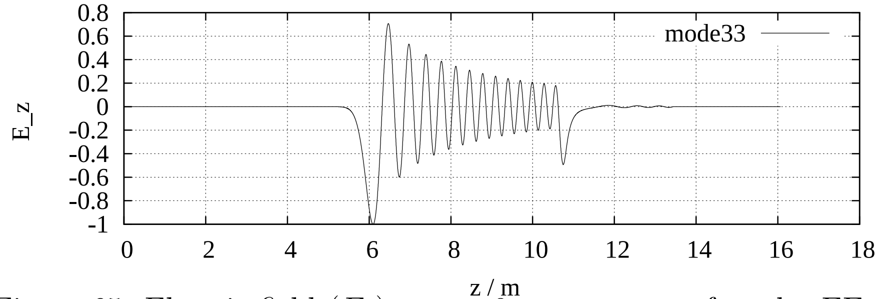

Figure 65: Electric field (E_z) at $r = 0$ cm versus z of mode: EE-33

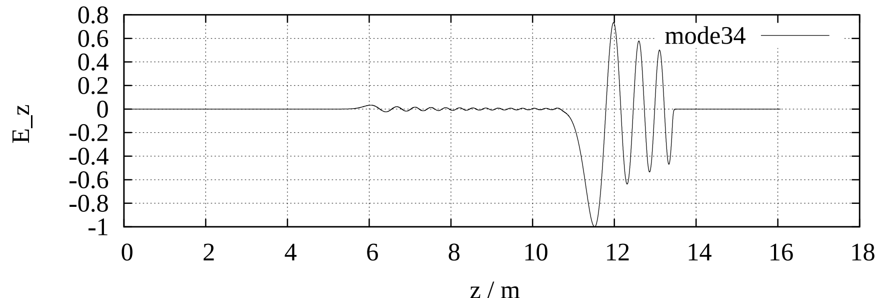

Figure 66: Electric field (E_z) at $r = 0$ cm versus z of mode: EE-34

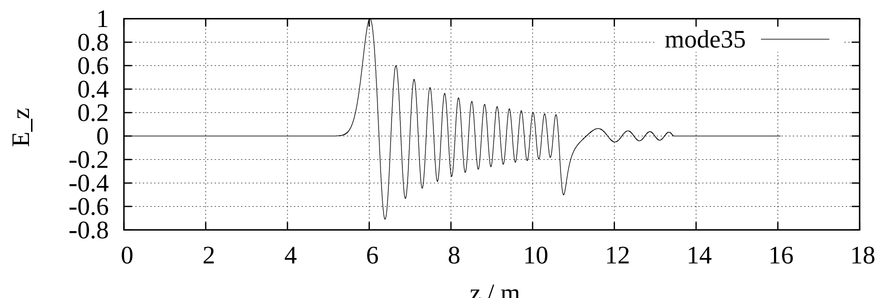

Figure 67: Electric field (E_z) at $r = 0$ cm versus z of mode: EE-35

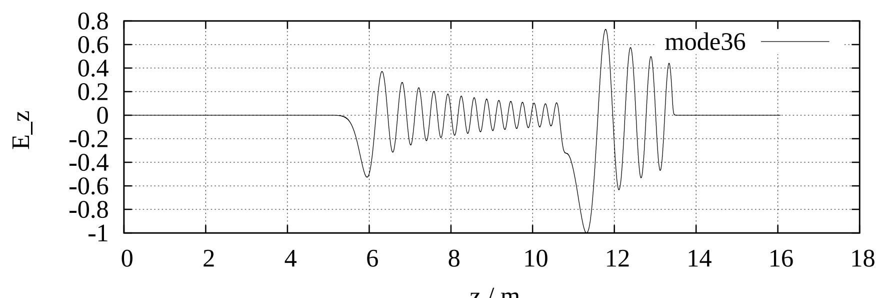

Figure 68: Electric field (E_z) at $r = 0$ cm versus z of mode: EE-36

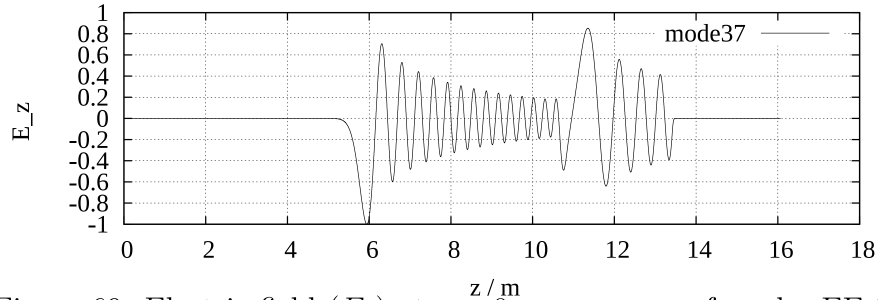

Figure 69: Electric field (E_z) at $r = 0$ cm versus z of mode: EE-37

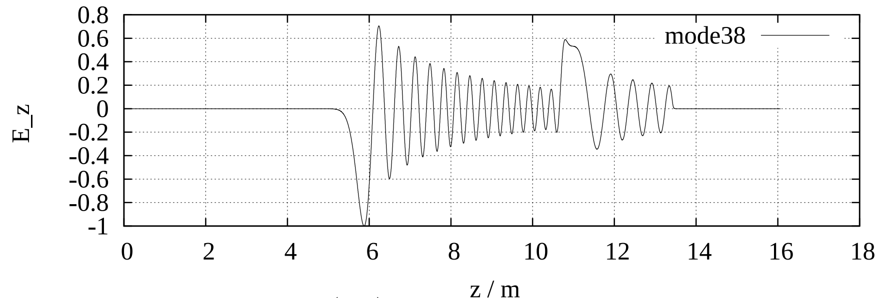

Figure 70: Electric field (E_z) at $r = 0$ cm versus z of mode: EE-38

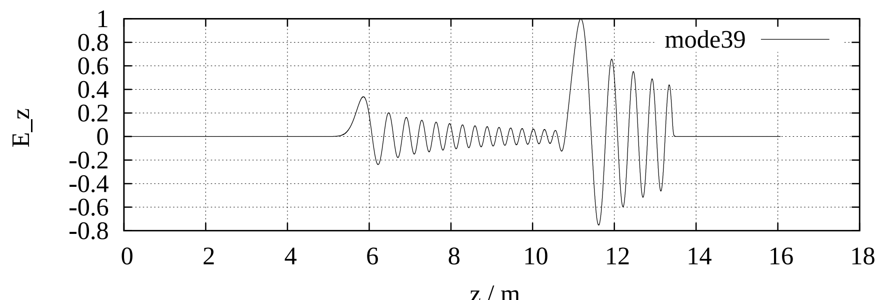

Figure 71: Electric field (E_z) at $r = 0$ cm versus z of mode: EE-39

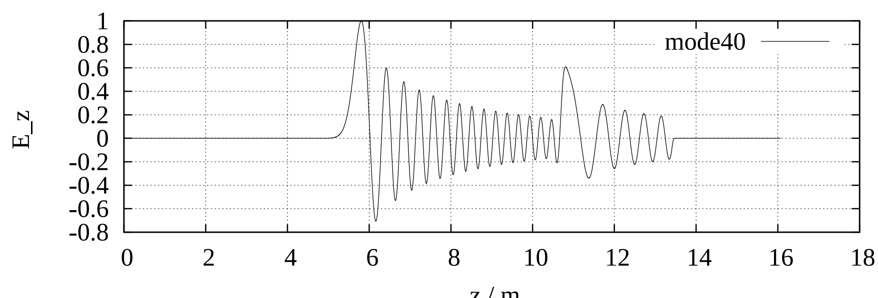

Figure 72: Electric field (E_z) at $r = 0$ cm versus z of mode: EE-40

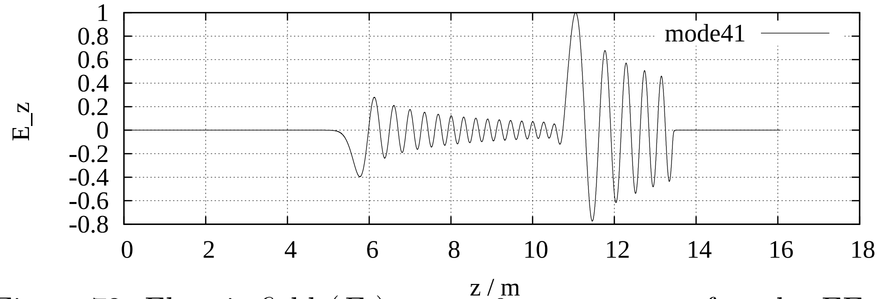

Figure 73: Electric field (E_z) at $r = 0$ cm versus z of mode: EE-41

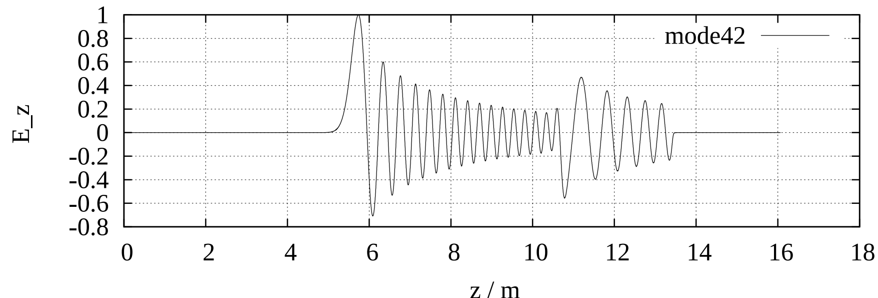

Figure 74: Electric field (E_z) at $r = 0$ cm versus z of mode: EE-42

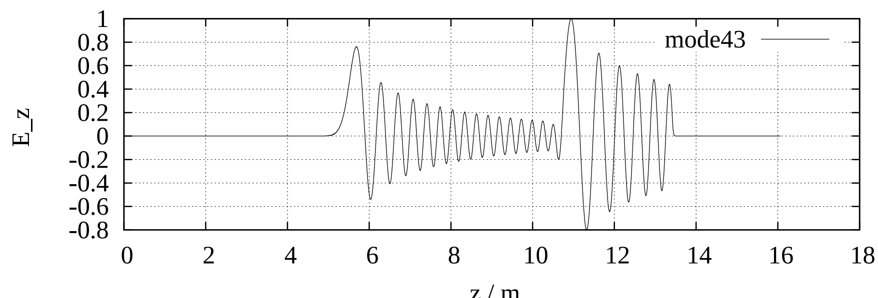

Figure 75: Electric field (E_z) at $r = 0$ cm versus z of mode: EE-43

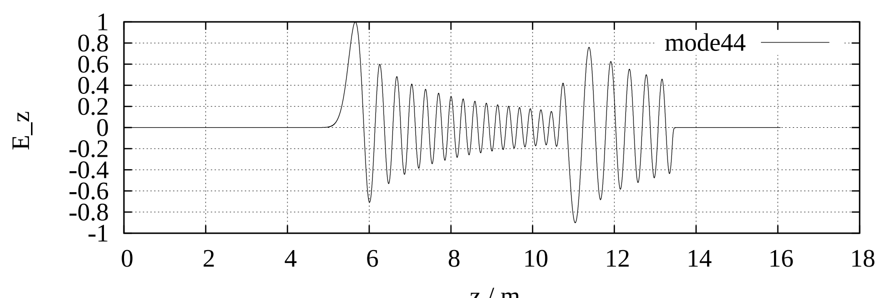

Figure 76: Electric field (E_z) at $r = 0$ cm versus z of mode: EE-44

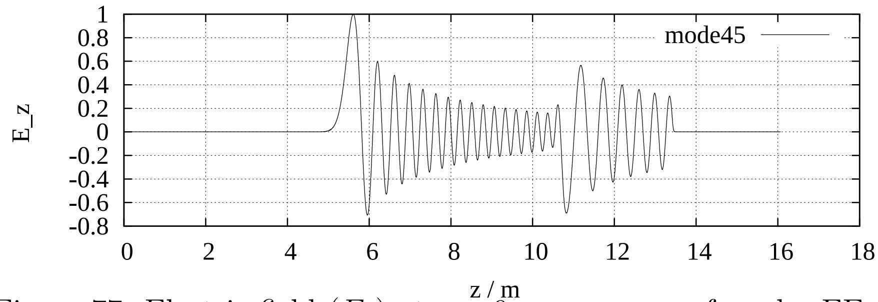

Figure 77: Electric field (E_z) at $r = 0$ cm versus z of mode: EE-45

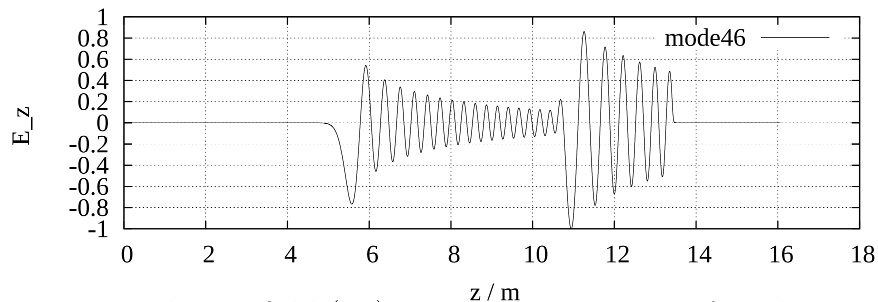

Figure 78: Electric field (E_z) at $r = 0$ cm versus z of mode: EE-46

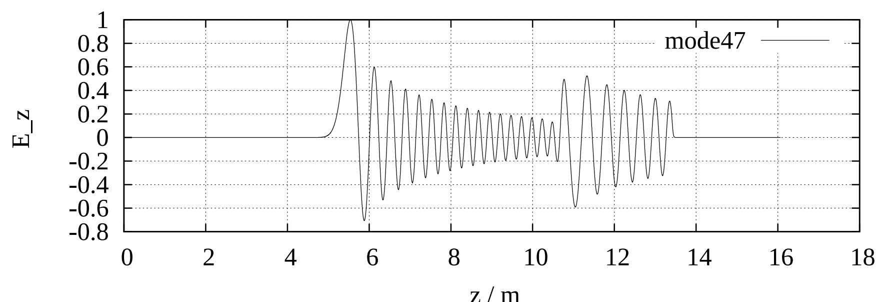

Figure 79: Electric field (E_z) at $r = 0$ cm versus z of mode: EE-47

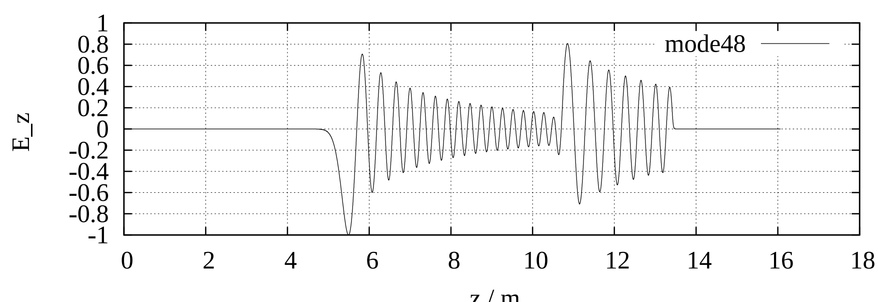

Figure 80: Electric field (E_z) at $r = 0$ cm versus z of mode: EE-48

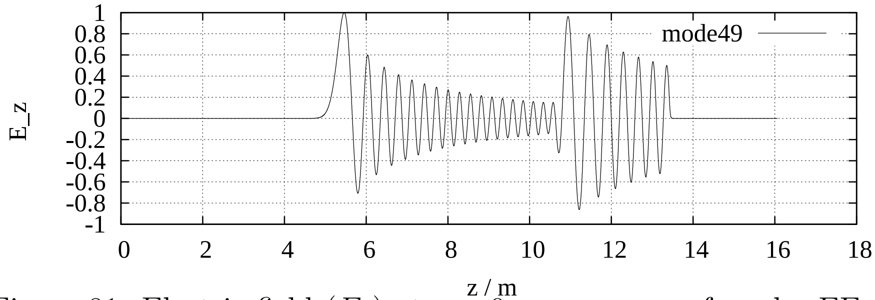

Figure 81: Electric field (E_z) at $r = 0$ cm versus z of mode: EE-49

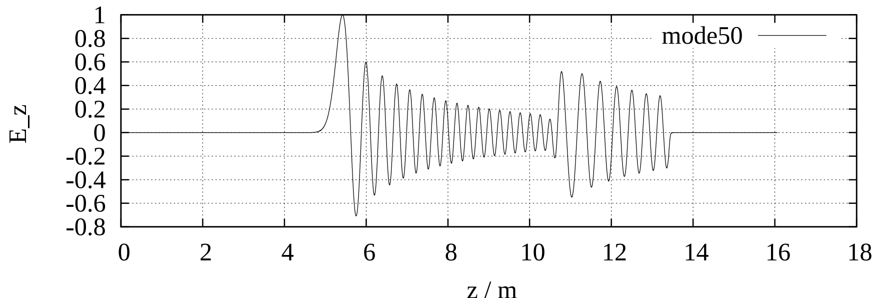

Figure 82: Electric field (E_z) at $r = 0$ cm versus z of mode: EE-50

B Electric fields of dipole modes

All electric fields are shown in arbitray units.

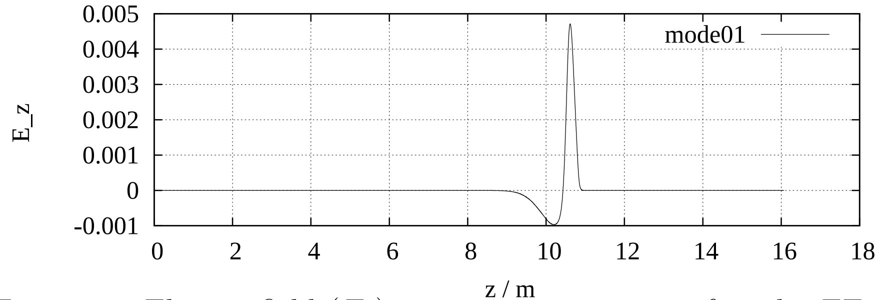

Figure 83: Electric field (E_z) at $r = 1$ cm versus z of mode: EE-01

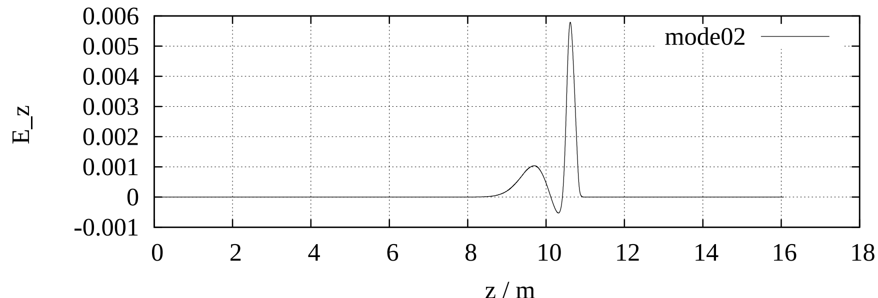

Figure 84: Electric field (E_z) at $r = 1$ cm versus z of mode: EE-02

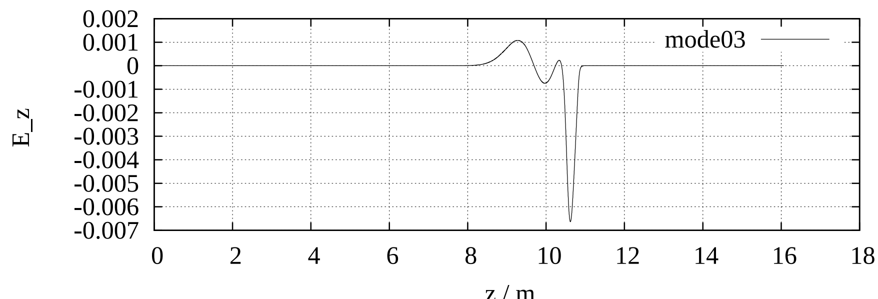

Figure 85: Electric field (E_z) at $r = 1$ cm versus z of mode: EE-03

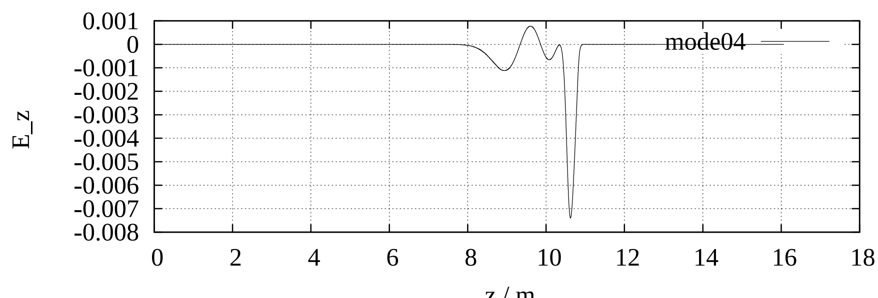

Figure 86: Electric field (E_z) at $r = 1$ cm versus z of mode: EE-04

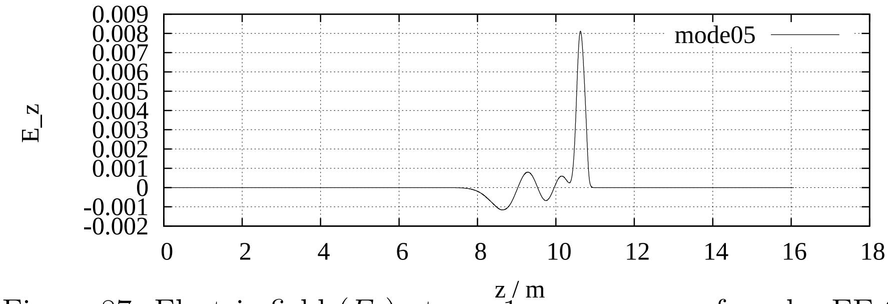

Figure 87: Electric field (E_z) at $r = 1$ cm versus z of mode: EE-05

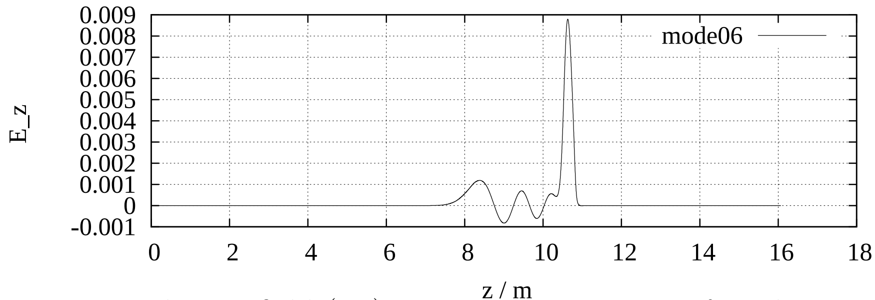

Figure 88: Electric field (E_z) at $r = 1$ cm versus z of mode: EE-06

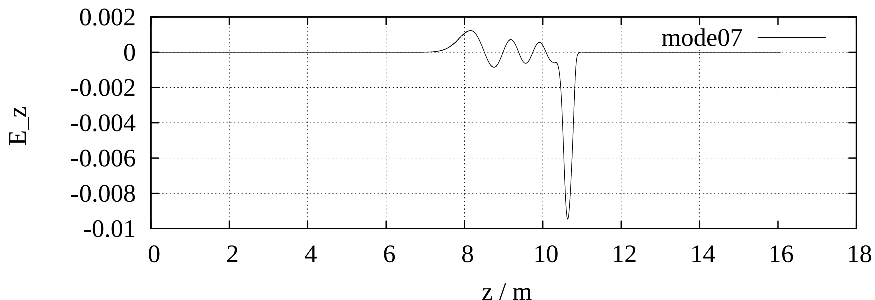

Figure 89: Electric field (E_z) at $r = 1$ cm versus z of mode: EE-07

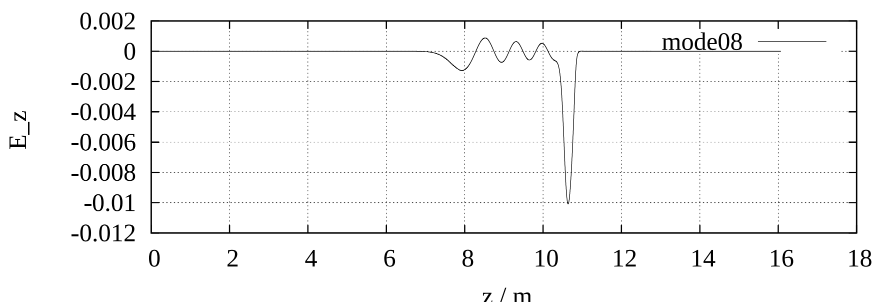

Figure 90: Electric field (E_z) at $r = 1$ cm versus z of mode: EE-08

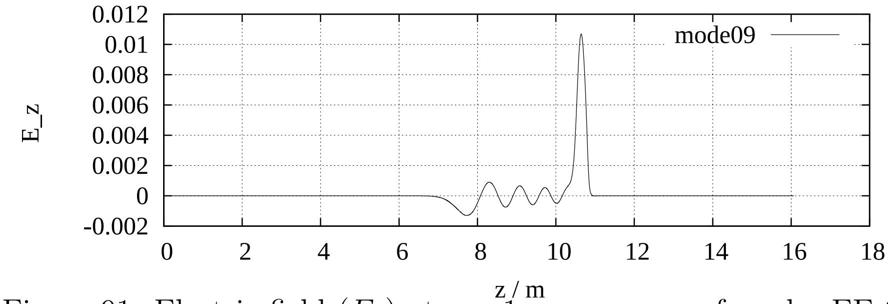

Figure 91: Electric field (E_z) at $r = 1$ cm versus z of mode: EE-09

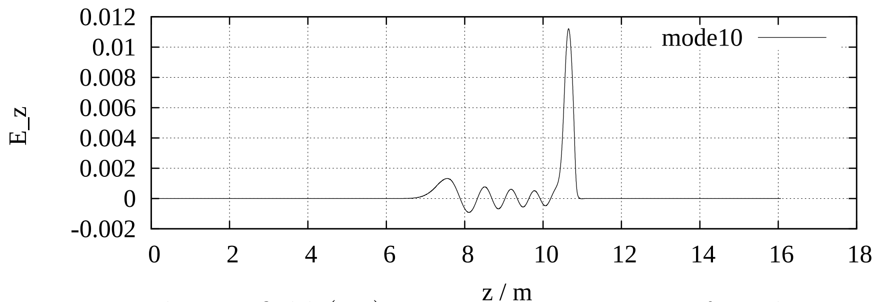

Figure 92: Electric field (E_z) at $r = 1$ cm versus z of mode: EE-10

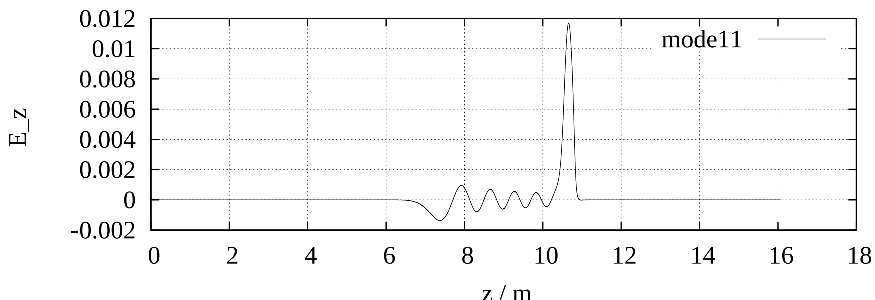

Figure 93: Electric field (E_z) at $r = 1$ cm versus z of mode: EE-11

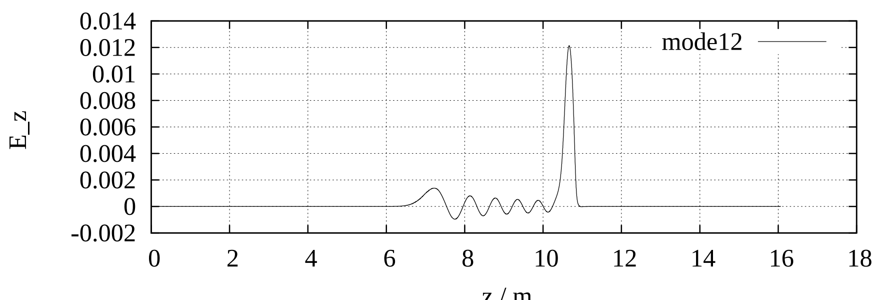

Figure 94: Electric field (E_z) at $r = 1$ cm versus z of mode: EE-12

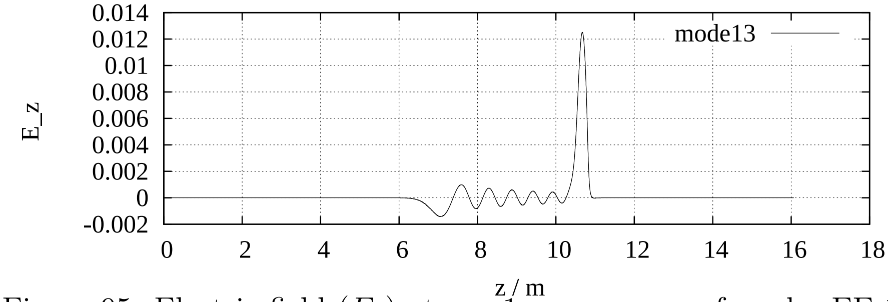

Figure 95: Electric field (E_z) at $r = 1$ cm versus z of mode: EE-13

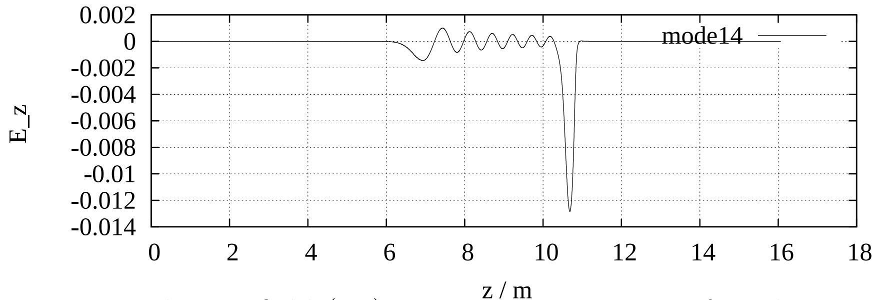

Figure 96: Electric field (E_z) at $r = 1$ cm versus z of mode: EE-14

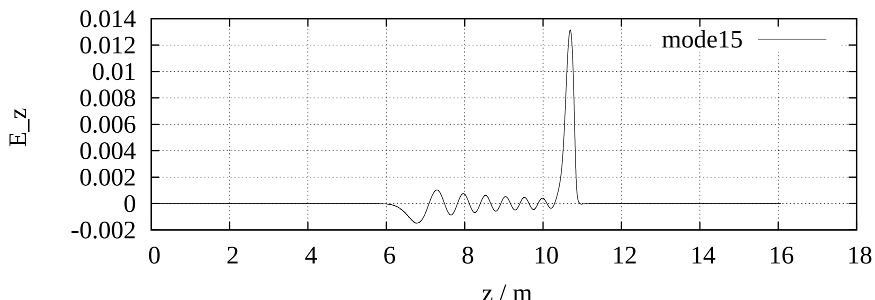

Figure 97: Electric field (E_z) at $r = 1$ cm versus z of mode: EE-15

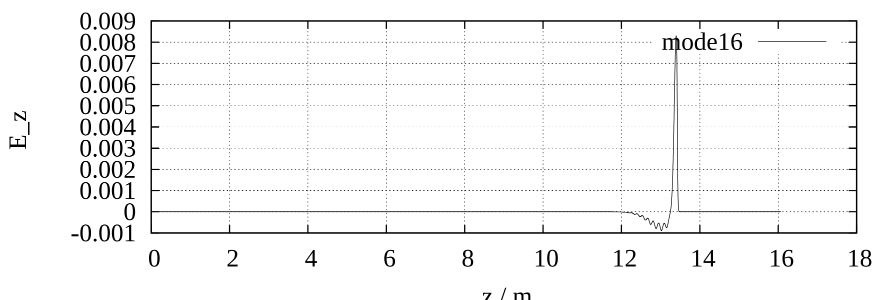

Figure 98: Electric field (E_z) at $r = 1$ cm versus z of mode: EE-16

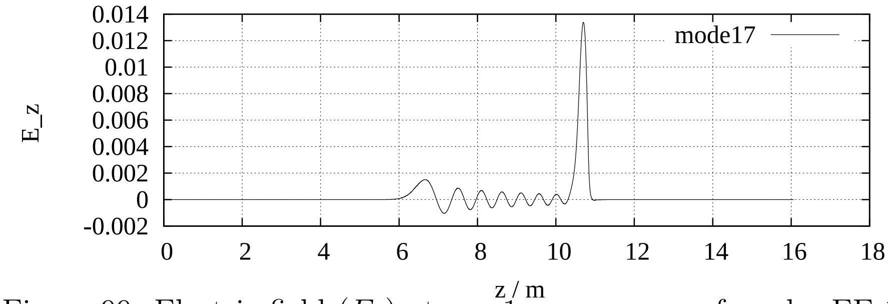

Figure 99: Electric field (E_z) at $r = 1$ cm versus z of mode: EE-17

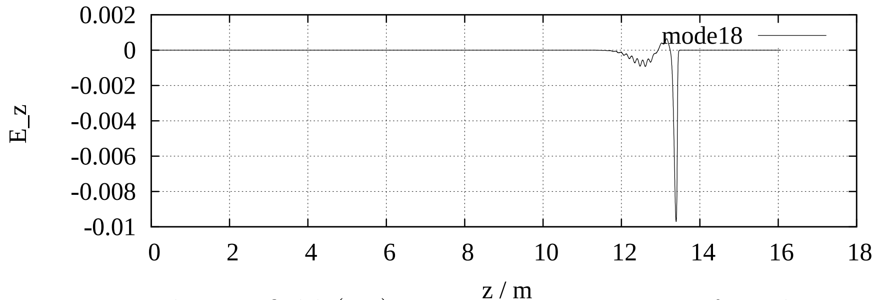

Figure 100: Electric field (E_z) at $r = 1$ cm versus z of mode: EE-18

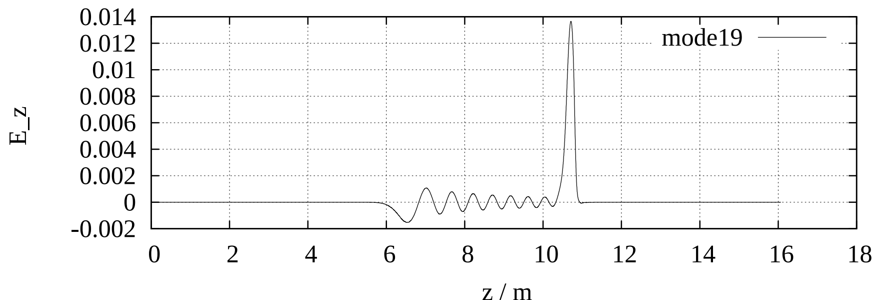

Figure 101: Electric field (E_z) at $r = 1$ cm versus z of mode: EE-19

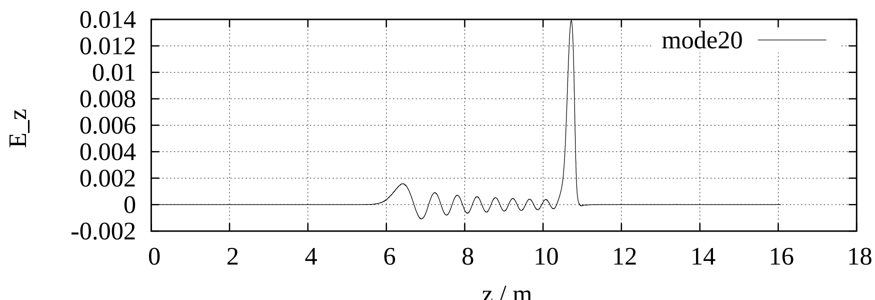

Figure 102: Electric field (E_z) at $r = 1$ cm versus z of mode: EE-20

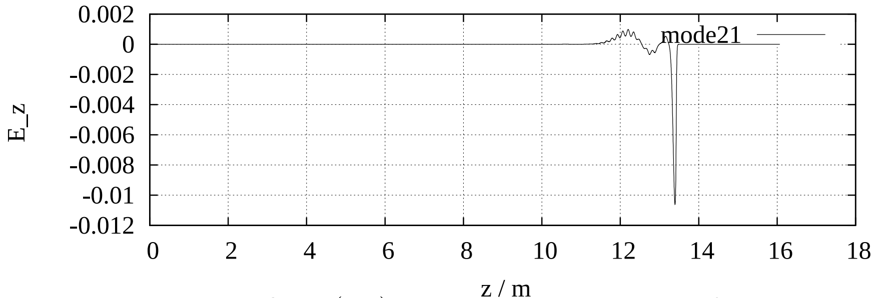

Figure 103: Electric field (E_z) at $r = 1$ cm versus z of mode: EE-21

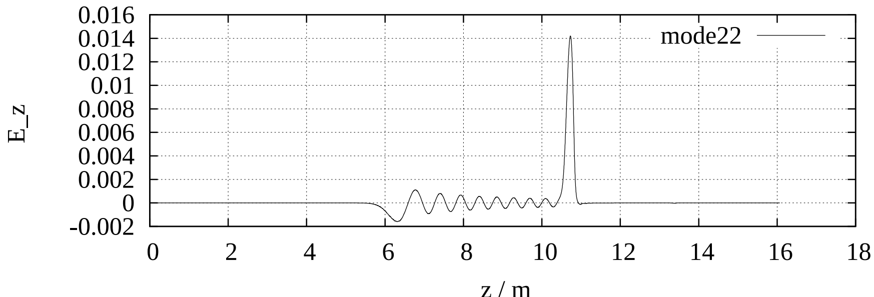

Figure 104: Electric field (E_z) at $r = 1$ cm versus z of mode: EE-22

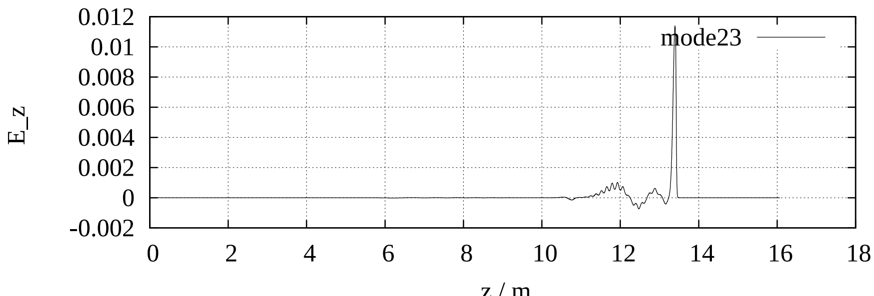

Figure 105: Electric field (E_z) at $r = 1$ cm versus z of mode: EE-23

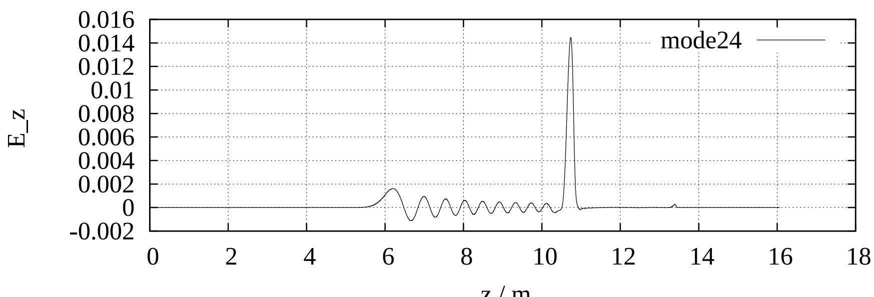

Figure 106: Electric field (E_z) at $r = 1$ cm versus z of mode: EE-24

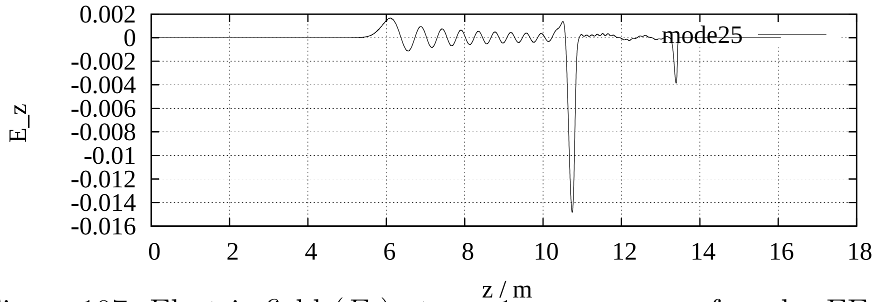

Figure 107: Electric field (E_z) at $r = 1$ cm versus z of mode: EE-25

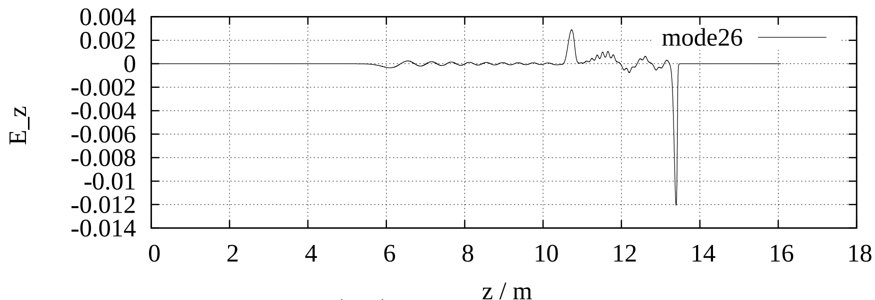

Figure 108: Electric field (E_z) at $r = 1$ cm versus z of mode: EE-26

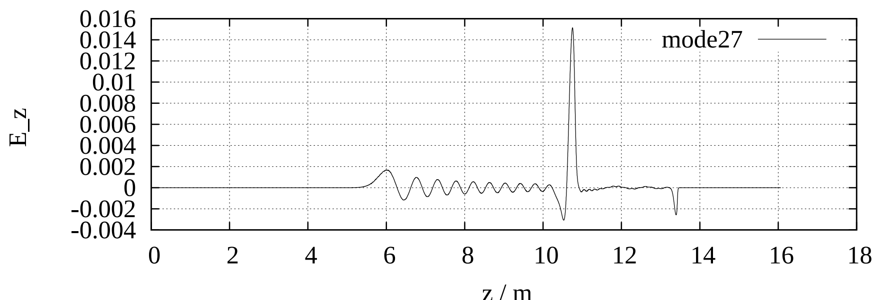

Figure 109: Electric field (E_z) at $r = 1$ cm versus z of mode: EE-27

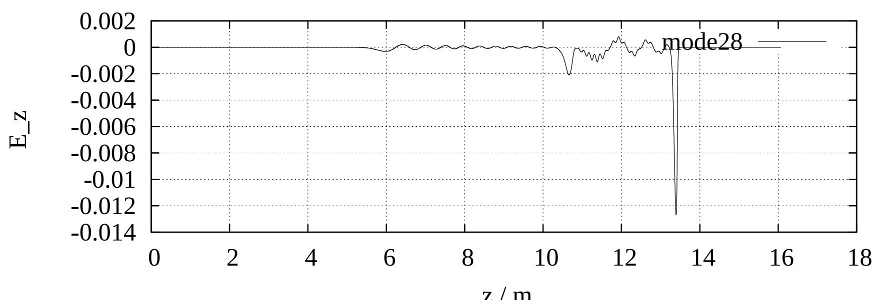

Figure 110: Electric field (E_z) at $r = 1$ cm versus z of mode: EE-28

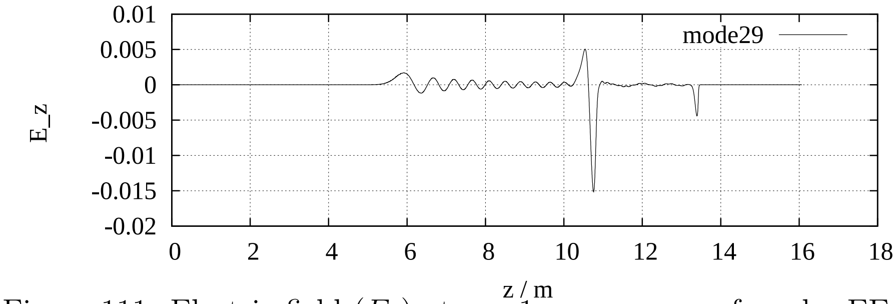

Figure 111: Electric field (E_z) at $r = 1$ cm versus z of mode: EE-29

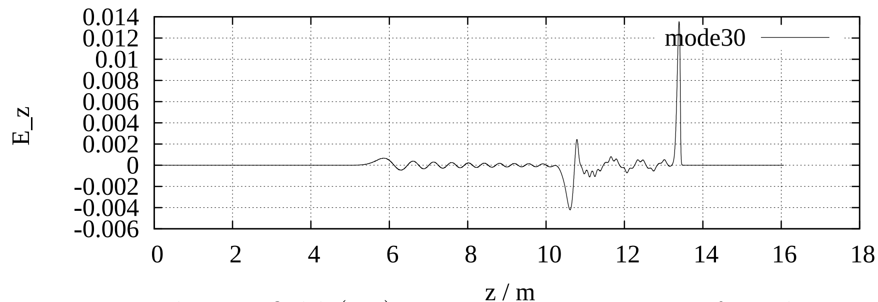

Figure 112: Electric field (E_z) at $r = 1$ cm versus z of mode: EE-30

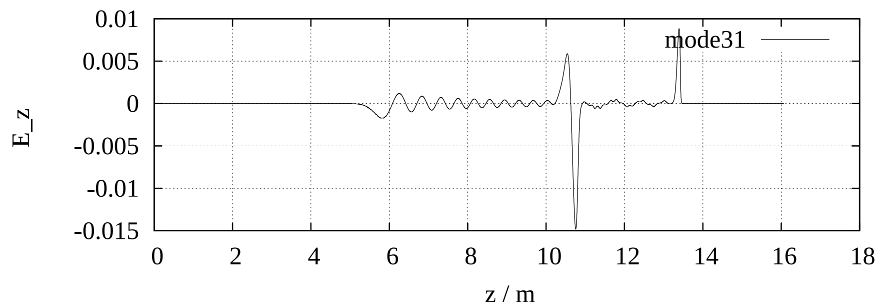

Figure 113: Electric field (E_z) at $r = 1$ cm versus z of mode: EE-31

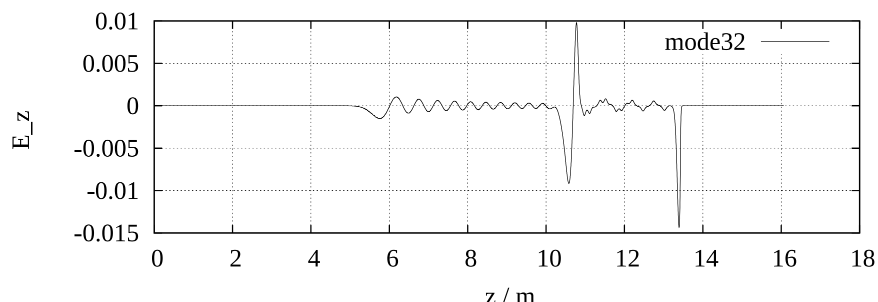

Figure 114: Electric field (E_z) at $r = 1$ cm versus z of mode: EE-32

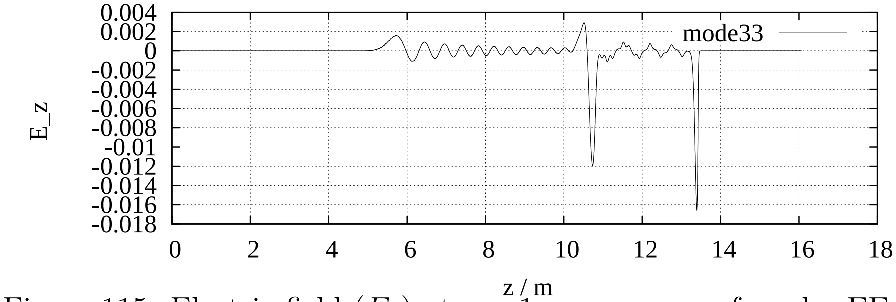

Figure 115: Electric field (E_z) at $r = 1$ cm versus z of mode: EE-33

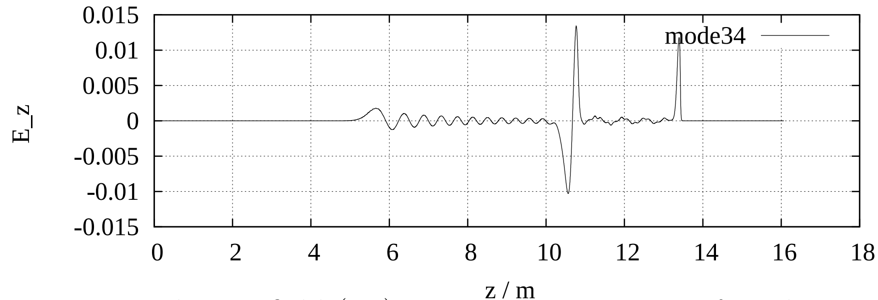

Figure 116: Electric field (E_z) at $r = 1$ cm versus z of mode: EE-34

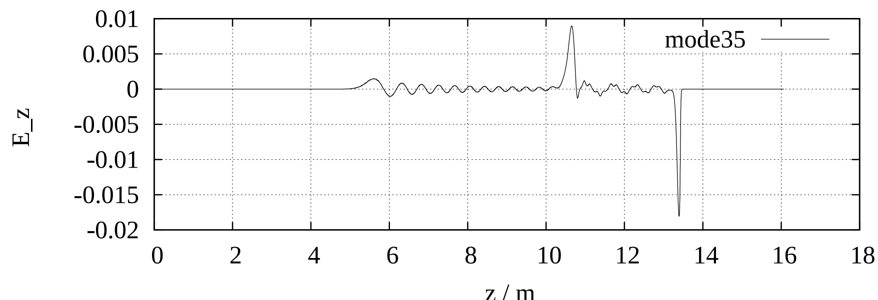

Figure 117: Electric field (E_z) at $r = 1$ cm versus z of mode: EE-35

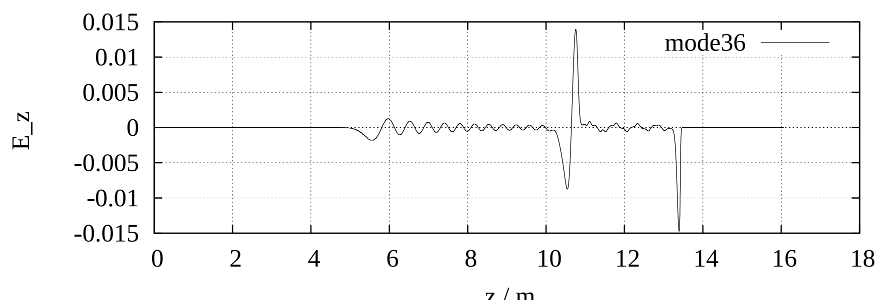

Figure 118: Electric field (E_z) at $r = 1$ cm versus z of mode: EE-36

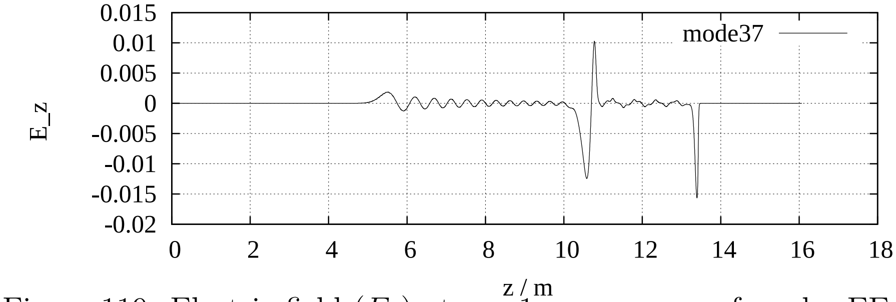

Figure 119: Electric field (E_z) at $r = 1$ cm versus z of mode: EE-37

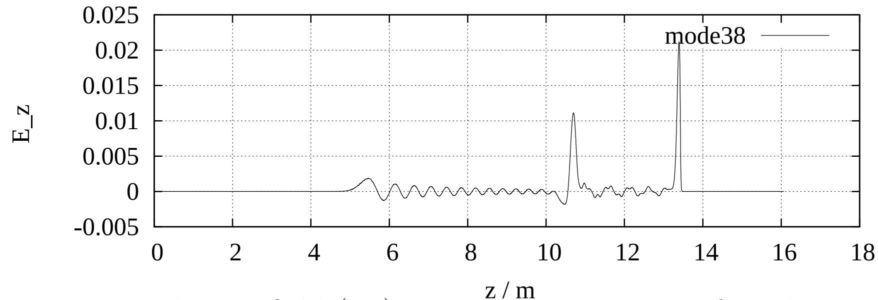

Figure 120: Electric field (E_z) at $r = 1$ cm versus z of mode: EE-38

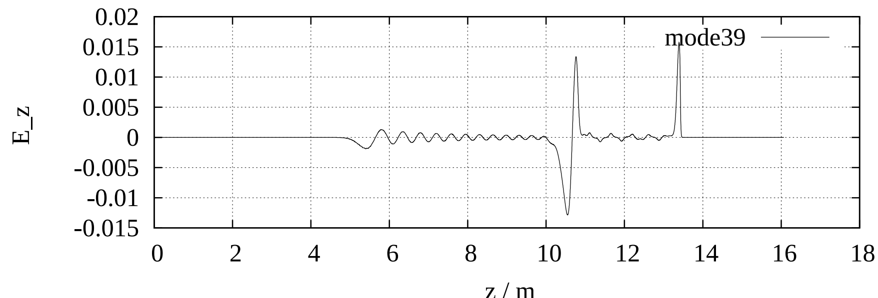

Figure 121: Electric field (E_z) at $r = 1$ cm versus z of mode: EE-39

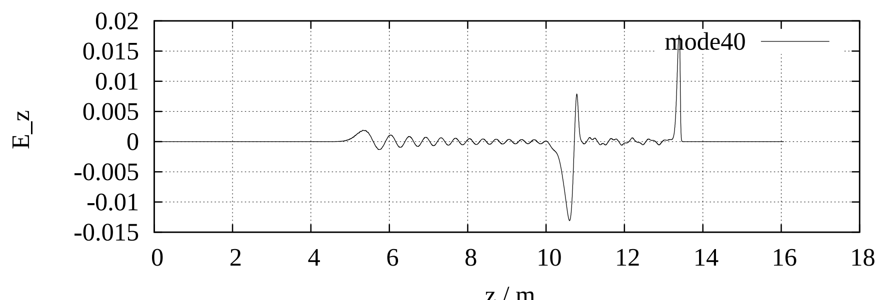

Figure 122: Electric field (E_z) at $r = 1$ cm versus z of mode: EE-40

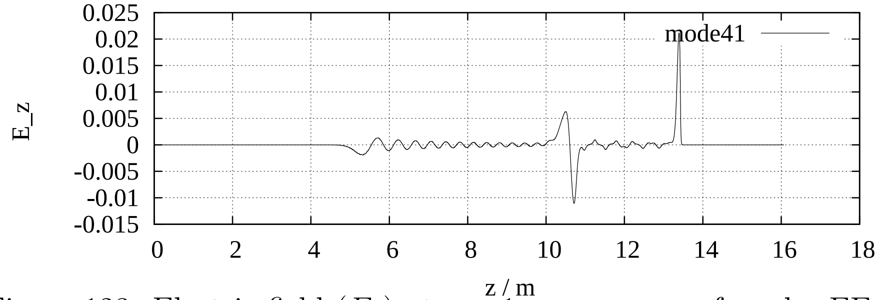

Figure 123: Electric field (E_z) at $r = 1$ cm versus z of mode: EE-41

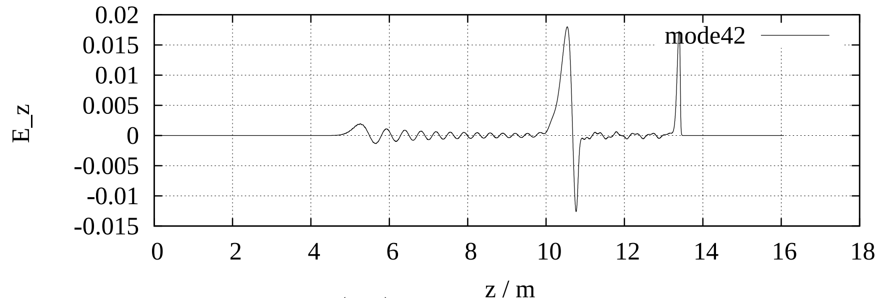

Figure 124: Electric field (E_z) at $r = 1$ cm versus z of mode: EE-42

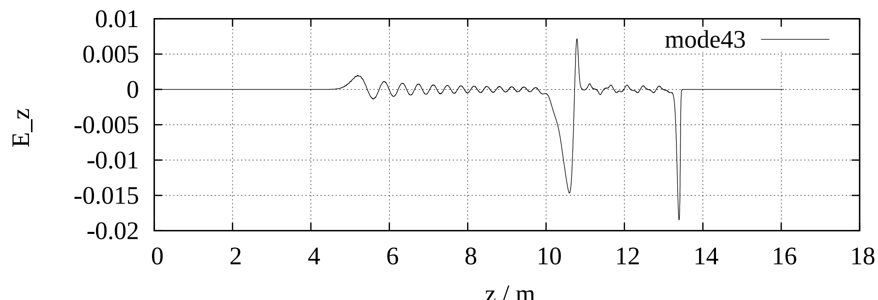

Figure 125: Electric field (E_z) at $r = 1$ cm versus z of mode: EE-43

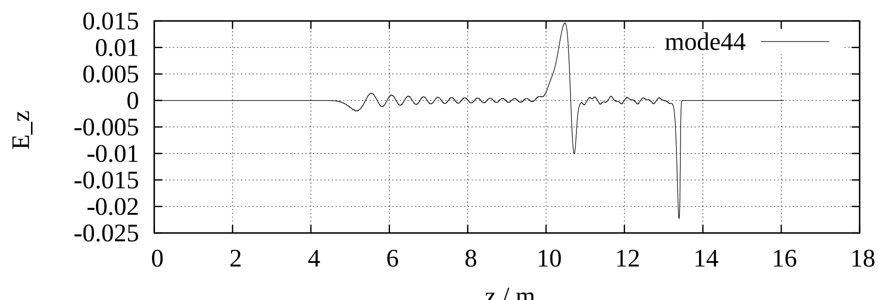

Figure 126: Electric field (E_z) at $r = 1$ cm versus z of mode: EE-44

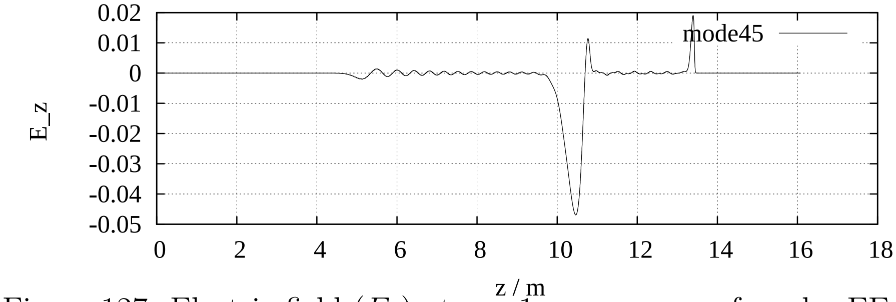

Figure 127: Electric field (E_z) at $r = 1$ cm versus z of mode: EE-45

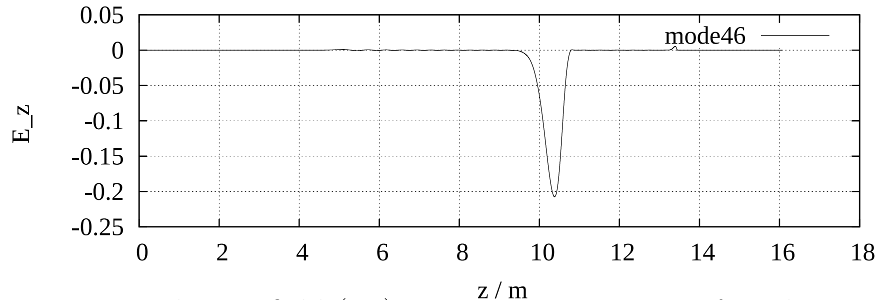

Figure 128: Electric field (E_z) at $r = 1$ cm versus z of mode: EE-46

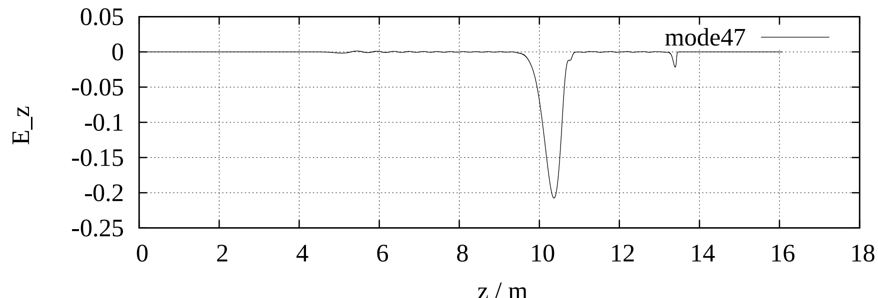

Figure 129: Electric field (E_z) at $r = 1$ cm versus z of mode: EE-47

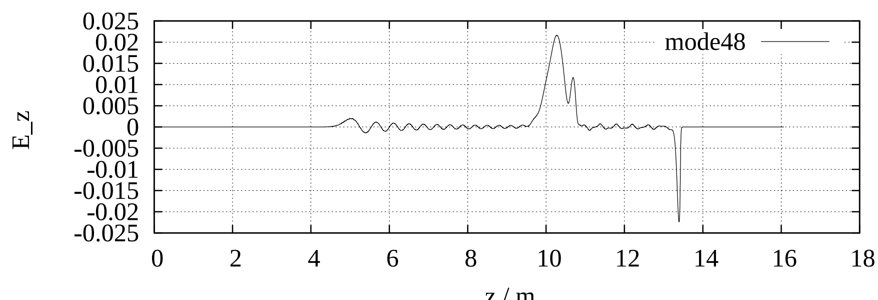

Figure 130: Electric field (E_z) at $r = 1$ cm versus z of mode: EE-48

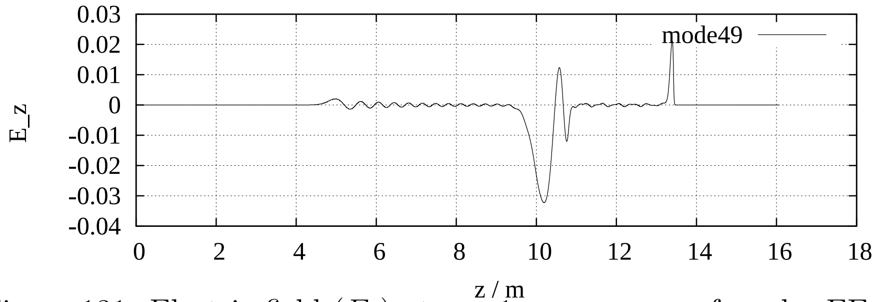

Figure 131: Electric field (E_z) at $r = 1$ cm versus z of mode: EE-49

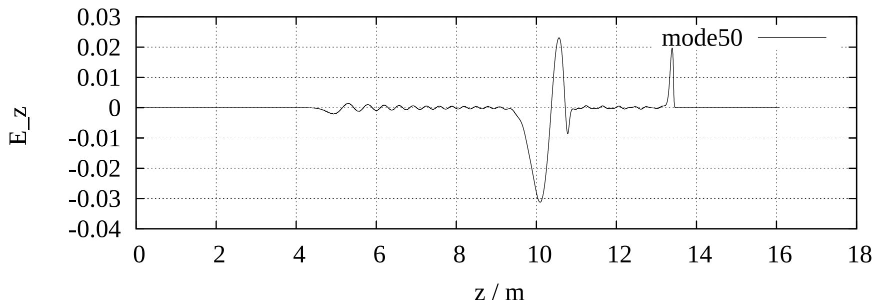

Figure 132: Electric field (E_z) at $r = 1$ cm versus z of mode: EE-50